Journal of the Meteorological Society of Japan, Vol. 87, No. 4, pp. 635–663, 2009.
DOI:10.2151/jmsj.87.635

Growth Rate, Seasonal, Synoptic, Diurnal Variations and Budget of Methane in the Lower Atmosphere

Prabir K. PATRA, Masayuki TAKIGAWA, Kentaro ISHIJIMA

Frontier Research Center for Global Change, JAMSTEC, Yokohama, Japan

Byoung-Choel CHOI[1]**,**

Korea Meteorological Administration, Seoul, Republic of Korea

Derek CUNNOLD

EAS, Georgia Institute of Technology, Atlanta, Georgia, USA

Edward J. DLUGOKENCKY

NOAA Earth System Research Laboratory, Boulder, Colorado, USA

Paul FRASER

Centre for Australian Weather and Climate Research, CSIRO Marine and Atmospheric Research, Victoria, Australia

Angel J. GOMEZ-PELAEZ

Izana Atmospheric Research Center, Agencia Estatal de Meteorologia, Santa Cruz de Tenerife, Spain

Tae-Young GOO, Jeong-Sik KIM

Korea Meteorological Administration, Seoul, Republic of Korea

Paul KRUMMEL

Centre for Australian Weather and Climate Research, CSIRO Marine and Atmospheric Research, Victoria, Australia

Ray LANGENFELDS

CSIRO Marine and Atmospheric Research, Victoria, Australia

Corresponding author: Prabir K. Patra, Frontier Research Center for Global Change, JAMSTEC, Yokohama 236-0001, Japan.
E-mail: prabir@jamstec.go.jp

1 Present affiliation: Regional Office for Asia and the South-West Pacific, World Meteorological Organization (WMO), Geneva 2, Switzerland.

Frank MEINHARDT

Umweltbundesamt—Federal Environment Agency, Langen, Germany

Hitoshi MUKAI

CGER, National Institute for Environmental Studies, Tsukuba, Japan

Simon O'DOHERTY

School of Chemistry, University of Bristol, Cantock's Close, UK

Ronald G. PRINN

EAPS/CGCS/JPSPGC, Massachusetts Institute of Technology, Cambridge, Massachusetts, USA

Peter SIMMONDS

School of Chemistry, University of Bristol, Cantock's Close, UK

Paul STEELE

Centre for Australian Weather and Climate Research, CSIRO Marine and Atmospheric Research, Victoria, Australia

Yasunori TOHJIMA

CGER, National Institute for Environmental Studies, Tsukuba, Japan

Kazuhiro TSUBOI

AED/GEMD, Japan Meteorological Agency, Tokyo, Japan

Karin UHSE

Umweltbundesamt—Federal Environment Agency, Langen, Germany

Ray WEISS

Scripps Institution of Oceanography, La Jolla, California, USA

Doug WORTHY

Environment Canada, Toronto, Canada

and

Takakiyo NAKAZAWA

CAOS, Graduate School of Studies, Tohoku University, Sendai, Japan

Frontier Research Center for Global Change, JAMSTEC, Yokohama, Japan

(Manuscript received 25 August 2009, in final form 1 April 2009)

Abstract

We have used an AGCM (atmospheric general circulation model)-based Chemistry Transport Model (ACTM) for the simulation of methane (CH_4) in the height range of earth's surface to about 90 km. The model simulations are compared with measurements at hourly, daily, monthly and interannual time scales by filtering or averaging all the timeseries appropriately. From this model-observation comparison, we conclude that the recent (1990–2006) trends in growth rate and seasonal cycle at most measurement sites can be fairly successfully modeled by using existing knowledge of CH_4 flux trends and seasonality. A large part of the interannual variability (IAV) in CH_4 growth rate is apparently controlled by IAV in atmospheric dynamics at the tropical sites and forest fires in the high latitude sites. The flux amplitudes are optimized with respect to the available hydroxyl radical (OH) distribution and model transport for successful reproduction of latitudinal and longitudinal distribution of observed CH_4 mixing ratio at the earth's surface. Estimated atmospheric CH_4 lifetime in this setup is 8.6 years. We found a small impact (less than 0.5 ppb integrated over 1 year) of OH diurnal variation, due to temperature dependence of reaction rate coefficient, on CH_4 simulation compared to the transport related variability (order of $\pm$15 ppb at interannual timescales). Model-observation comparisons of seasonal cycles, synoptic variations and diurnal cycles are shown to be useful for validating regional flux distribution patterns and strengths. Our results, based on two emission scenarios, suggest reduced emissions from temperate and tropical Asia region (by 13, 5, 3 Tg-CH_4 for India, China and Indonesia, respectively), and compensating increase (by 9, 9, 3 Tg-CH_4 for Russia, United States and Canada, respectively) in the boreal Northern Hemisphere (NH) are required for improved model-observation agreement.

1. Introduction

Methane has a global warming potential of 25 (over 100 year time horizon) with respect to carbon dioxide (CO_2) on per mass emitted basis, and plays a significant role in controlling oxidizing capacity of the troposphere (Houghton et al. 1990 and references therein). The records of past atmospheric composition show variations of CH_4 abundance in the atmosphere is controlled by both natural and anthropogenic activities (e.g., Rasmussen and Khalil 1984; Nakazawa et al. 1993; Etheridge et al. 1998; Ferretti et al. 2005). Over the last 20 years, the CH_4 growth rate has been varying significantly from year to year (Steele et al. 1992; Dlugokencky et al. 1998; Cunnold et al. 2002; Morimoto et al. 2006), and a large decrease was observed at all sites around 2000 (Dlugokencky et al. 2003; Simpson et al. 2006; this study). Due to the measurements at large number of sites, the causes for these changes in atmospheric CH_4 can be analyzed by inverse model estimations of surface fluxes (Hein et al. 1997; Houweling et al. 1999; Mikaloff-Fletcher et al. 2004; Chen and Prinn 2006; Bousquet et al. 2006). For example, interannual variability (IAV) in CH_4 emission from wetlands are suggested to be responsible for producing large IAVs in atmospheric CH_4 variability (Bousquet et al. 2006 and references therein), which is commonly linked to the IAV or trends in surface temperature of the Northern Hemisphere (NH) boreal region (e.g., Walter et al. 2001). Methane emission due to forest fires is another known factor for controlling IAV in atmospheric CH_4 (Langenfelds et al. 2002; Morimoto et al. 2006; Simpson et al. 2006). The IAV in CH_4 growth rate is also attributed to anthropogenic activity such as those occurred in CH_4 emission from Russia during the post Soviet Union era (Dlugokencky et al. 1998).

The inverse model estimations of surface fluxes and associated variability rely heavily on the forward transport model simulations. Methane forward simulation depends on surface emission distribution, model transport and chemical loss in the troposphere and stratosphere as well as the stratosphere-troposphere exchange (STE). Apart from the large uncertainty in the IAV and low predictability of OH concentrations due to climate variations and precursor species changes (Krol et al. 1998; Prinn et al. 2001; Manning et al. 2005), the hydroxyl radical (OH) absolute concentrations over certain location or between the hemispheres vary greatly between the 26 state-of-the-art Chemistry-Transport Models (CTMs), participating in a recently concluded intercomparison project (Dentener et al. 2006; Stevenson et al. 2006; Maarten Krol, pers. comm. 2008). Here we will use the monthly mean OH concentrations (without IAV) simulated by one of the participating models CHASER, developed for studying atmospheric environment and radiative forcing (Sudo et al. 2002). The estimated CH_4 lifetime for CHASER model

(~8.4 years) is close to the multimodel mean of 8.67 ± 1.32 (1σ) years and also for ozone budgets (Stevenson et al. 2006), and thus can be considered representative of the current state-of-the-art CTMs. Similarly, there is also uncertainty in CH_4 emissions as estimated using the data gathered by multiple research groups for different regions or emission types (e.g., Fung et al. 1991; Olivier and Berdowski 2001). A balance between the three (surface emission, total loss, and exchange with the stratosphere) is required to maintain the mass balance of CH_4 in the troposphere.

A large number of studies have explored the role of transport and emissions on the simulation of IAV in CH_4 growth rate, seasonal cycles and daily scale variations (e.g., Fung et al. 1991; Saeki et al. 1998; Houweling et al. 2000, 2006; Warwick et al. 2002; Wang et al. 2004; Dentener et al. 2003; Chen and Prinn 2005; Fiore et al. 2006). It is generally agreed that the use of realistic meteorology, such as observed/analyzed winds, is important for capturing various aspects of the observed CH_4 variations. However, the synoptic and diurnal variations in CH_4 have not been studied in detail. Some analyses of hourly to weekly time scale CH_4 variability have been conducted using model-observation comparisons, which reiterated the importance of IAV meteorology for simulating CH_4 variations (Worthy et al. 1998; Tohjima et al. 2002; Chen and Prinn 2005). It is still challenging to match the model simulated seasonal cycle with the individual flask measurements (e.g., Wang et al. 2004; Chen and Prinn 2005; Fiore et al. 2006) without the use of inverse model estimated surface CH_4 fluxes. An inversion approach will, by design, improve the match with observations, but not necessarily for the right reason (i.e., process-level understanding can still be lacking). One commonly used emission type, i.e., emission due to rice cultivation, as used in the forward transport models (40–100 Tg-CH_4 yr^{-1}) does not comply well with recent advancements made in better constraining this flux in the range of 15–42 Tg-CH_4 yr^{-1} (Yan et al. 2008 and references therein).

We carry out the forward simulation of CH_4 based on two optimal emission scenarios, 3-dimensional OH and chlorine (Cl) radical distribution climatologies, and IAV meteorology using the Center for Climate System Research/National Institute for Environmental Studies/Frontier Research Center for Global Change (CCSR/NIES/FRCGC) atmospheric general circulation model (AGCM) based CTM [hereafter, ACTM]. The additional loss terms due to stratospheric Cl and excited state oxygen (O^1D) chemistry are considered critical for ACTM CH_4 simulation since this model covers the height range of approximately 0–90 km. This is in contrast with most other CTM based forward simulations which parameterize the stratospheric loss term by defining a climatological stratospheric CH_4 distribution or ignore some radical chemistry. In this work we aim to address the following features of the ACTM transport and bottom-up CH_4 flux estimates by model-observation comparison of atmospheric CH_4 on a range of timescales:

1. Inter-annual variability in model simulations arise mainly from the ACTM transport in terms of the vertical transport locally and horizontal transport at regional/hemispheric scales. This is because the main CH_4 chemistry precursors (OH, Cl) are considered to be climatologically varying (no IAV), and fluxes have small interannual increases, less than 0.05% in the period 1990–1995 and even smaller afterwards (Table 1).
2. Seasonal cycle in atmospheric CH_4 is caused by the seasonality in emissions distributions and strengths, chemical loss, and seasonal changes in regional meteorology. Thus the model-observation comparison gives us confidence on overall validity of the combination of regional to sub-hemispherical scale CH_4 flux and ACTM chemistry-transport scheme.
3. Synoptic variation in CH_4 is controlled by the regional flux distribution and atmospheric transport at synoptic timescales. Thus model-data comparisons of atmospheric CH_4 timeseries are likely to provide information on regional source and sink strengths under the condition of realistic model transport.
4. Diurnal variation in CH_4 is likely to be controlled by local emissions and transport (e.g., diurnal variations in PBL mixing), providing us an indirect method for validating the ACTM modeling framework at the local scale, because the effect of OH diurnal variation on CH_4 loss is shown to be small (this study).

2. Model and data description

2.1 ACTM dynamics and chemistry setup

We have used the CCSR/NIES/FRCGC ACTM for simulating atmospheric CH_4 at hourly time intervals, a horizontal resolution of T42 spectral trun-

Table 1. Annual mean CH_4 emissions (Tg-CH_4) as used in the ACTM simulation (left two columns), atmospheric budget and sector-wise emission totals (3rd and 4th columns), and area-wise totals (right four columns) for E2 and E1 emission scenarios (see text).

Year	Total emission (E2)	Tropospheric Budget (E2)	Year 2000 (E2)	Top emission country (E2)	Aggr. Emission (E2)	Top emission country (E1)	Aggr. Emission (E1)
1988	569.4	**Anthropogenic***	**301.9**	Brazil	54.2	India	54.2
1989	570.6	Biofuel	16.0	USA	54.0	Brazil	53.7
1990	571.1	Fossil fuel	102.9	Russia	51.3	China	52.8
1991	571.7	Industrial	0.9	China	47.4	USA	44.8
1992	572.3	Animal + Fire	119.3	India	41.1	Russia	42.9
1993	572.9	Waste	62.7	Indonesia	30.1	Indonesia	33.2
1994	573.4	**Biogenic****	**273.0**	Canada	17.3	Canada	14.4
1995	574.0	Termites	20.5	Argentina	14.9	Argentina	14.2
1996	574.3	Biomass Burn	59.8	Australia	11.7	Thailand	13.5
1997	574.7	Rice	39.4	Thailand	10.7	Australia	10.0
1998	574.1	Swamps	104.4	Zaire	8.9	Nigeria	8.7
1999	574.5	Bogs	40.2	Nigeria	8.7	Vietnam	8.4
2000	575.0	Tundra	8.7	Sudan	8.6	Zaire	8.3
2001	574.7	**Sinks**	**~580**	Mexico	8.1	Sudan	8.1
2002	574.2	Trop. Loss	551	Venezuela	7.1	Mexico	7.8
2003	574.9	Strat. Loss	29	Ukraine	6.6	Pakistan	7.1
2004	574.6	NH Loss	334	Vietnam	6.5	Venezuela	7.0
2005	574.8	SH Loss	246	Pakistan	6.4	Ukraine	6.6
2006	574.8	**Atmos. Burden**	**4999**	Peru	6.3	Peru	6.2

*Total EDGAR anthropogenic emissions have been normalized to a value of 301.9 Tg-CH_4 yr^{-1} for the year 2000 by including following sources; B-type (Biofuel): B10 + B20 + B30 + B40 + B51; F-type (Fossil fuel): F10 + F20 + F30 + F40 + F51 + F54 + F57 + F58 + F70 + F80 + F90; I-type (Industrial processes): I10 + I30; L-type (Animal + Fire): L20 + L30 + L41 + L42 + L43 + L44 + L47; W-type (Waste handling): W10 + W20 + W30 + W40. Please refer to EDGAR documentation for further details [Olivier and Berdowski, 2001; www.mnp.nl, path: edgar/documentation/definitions].

**Multipliers for GISS CH_4 fluxes due to Termite, Biomass Burning, Rice Cultivation, Tundra, Swamps and Bogs are 0.77, 0.49, 0.75, 1, 1.83 and 1.3 for E1 scenario, and 0.77, 0.49, 0.37, 2, 2 and 1 for E2 scenario, respectively.

cation (~2.8 × 2.8°) and 67 sigma-pressure vertical layers (surface—about 90 km). The model transport is nudged with NCEP/DOE AMIP-II reanalysis (Kanamitsu et al. 2002; www.cpc.ncep.noaa.gov, path: products/wesley/reanalysis2) horizontal winds and temperature at 6-hourly time interval for incorporating IAV dynamics in ACTM. The ACTM has been widely used for simulating various atmospheric species, such as CO_2, CH_4, sulfur hexafluoride (SF_6), nitrous oxide (N_2O), ^{222}radon, and studying the mechanisms of their short/long-term variabilities by comparing with measurements. ACTM simulation of non-reactive SF_6 is used for validating model transport in the synoptic to annual timescales (Patra et al. 2009), and also participated in international transport model intercomparison studies for CO_2 forward simulation, i.e., TransCom (Law et al. 2008; Patra et al. 2008). Un-

like SF_6 and CO_2, CH_4 has chemical loss in the troposphere to mesosphere height range due to the reaction with OH, Cl and O^1D radicals and photolysis by solar ultraviolet (UV) radiations. The latter has been ignored here, and the reactions along with the rate constants as modeled in ACTM are given below.

$$CH_4 + O^1D \rightarrow \text{Products} \quad (K_{O^1D} = 1.5 \times 10^{-10})$$

$$CH_4 + OH \rightarrow CH_3 + H_2O$$

$$(K_{OH} = 2.45 \times 10^{-12} \exp(-1775/T))$$

$$CH_4 + Cl \rightarrow CH_3 + HCl$$

$$(K_{Cl} = 7.3 \times 10^{-12} \exp(-1280/T))$$

The temperature dependent reaction rate coefficients (K) are taken from JPL synthesis report (Sander et al. 2006). The climatological monthly-mean OH concentrations are taken from a full tropospheric chemistry simulation in the troposphere (Sudo et al. 2002), and the stratospheric OH and Cl concentrations are obtained from a stratospheric chemistry model version representing the halogen loading corresponding to the year 2000 (Takigawa et al. 1999). The IAV in Cl over the period of our simulation is not considered. Concentration of O^1D is calculated online in ACTM using a climatological ozone distribution and AGCM calculated short-wave radiation at each model grid (Takigawa et al. 1999).

2.2 *Emission scenarios and tropospheric OH*

We used the natural/biogenic flux distributions from Goddard Institute for Space Studies (GISS) (Fung et al. 1991; Matthews and Fung 1987) after applying scaling factors to each individual component to produce an annual total of 273 Tg-CH_4 yr^{-1}; this flux varies month-to-month, but does not change from year to year for same month (referred to as cyclostationary or climatologically varying). The scaling/multiplication factor to individual flux types is selected based on the published literatures (e.g., Mikaloff-Fletcher et al. 2004; Houweling et al. 2006; Bousquet et al. 2006; Yan et al. 2008). Annual mean anthropogenic/industrial flux distributions are taken from the Emission Database for Global Atmospheric Research (EDGAR) inventory (Olivier and Berdowski 2001), and the total flux is scaled by a factor of 1.14 to match approximately the annual total anthropogenic emission trends recommended in EDGAR HYDE (History Database of the Global Environment). Since the HYDE database covers the period up to year 2000, the anthropogenic emissions are kept fairly constant at about 300 Tg-CH_4 yr^{-1} for the period 2000–2006. Global total values for all years are given in Table 1 for our preferred emission scenario (E2 case). Emission scenario E1 was used initially and optimized (emission scenario E2) by selecting different multipliers (see Table 1) for individual flux types to match seasonal cycles at a few NH high-latitude sites and interhemispheric gradient of atmospheric CH_4. The forward simulation results using the E2 emission scenarios are plotted and discussed as our *Control case*, unless specified otherwise of the E1 scenario. Total emission distributions of CH_4 at surface are shown in Fig. 1 during the boreal winter and summer seasons. We have omitted soil sink component in the simulations presented here. However, note that ACTM simulations with (annual total emission balanced by increasing anthropogenic emission) and without including soil sink showed markedly similar CH_4 seasonal cycle at all sites.

The absolute flux amount required to maintain global average growth rate depends primarily on OH field strength, troposphere-stratosphere exchange (STE) in the model. For instance STE in this version of ACTM works reasonably well to simulate SF_6 growth rate in the troposphere, when emission trend is matched with the increase in tropospheric abundance (Patra et al. 2009). The OH distribution used in CH_4 simulations has been verified for reproducing global average growth rate in methyl chloroform (MCF; CH_3CCl_3) using the Global Emission Inventory Activity (GEIA) database for the period up to 2000 (McCulloch and Midgley 2001). Figure 2 shows the model-observation comparison of daily-averaged MCF timeseries for the period of 1990–2000 at three Advanced Global Atmospheric Gases Experiment (AGAGE) network sites. The rise in concentration in the early 1990s followed by the decrease since about 1992 at Mace Head (MHD) and 1994 at Cape Grim (CGO) as well as the seasonal cycles are fairly well reproduced by ACTM (absolute difference less than 10 ppt between the background level concentrations at all sites). This overall match suggests the seasonality and global abundance of OH as used in this forward modeling framework are realistic. Further analysis using multiple tracers (e.g., MCF, CH_4) may be useful for verifying spatial distribution strength of OH, but is beyond the scope of this article. As stated earlier, no trend in

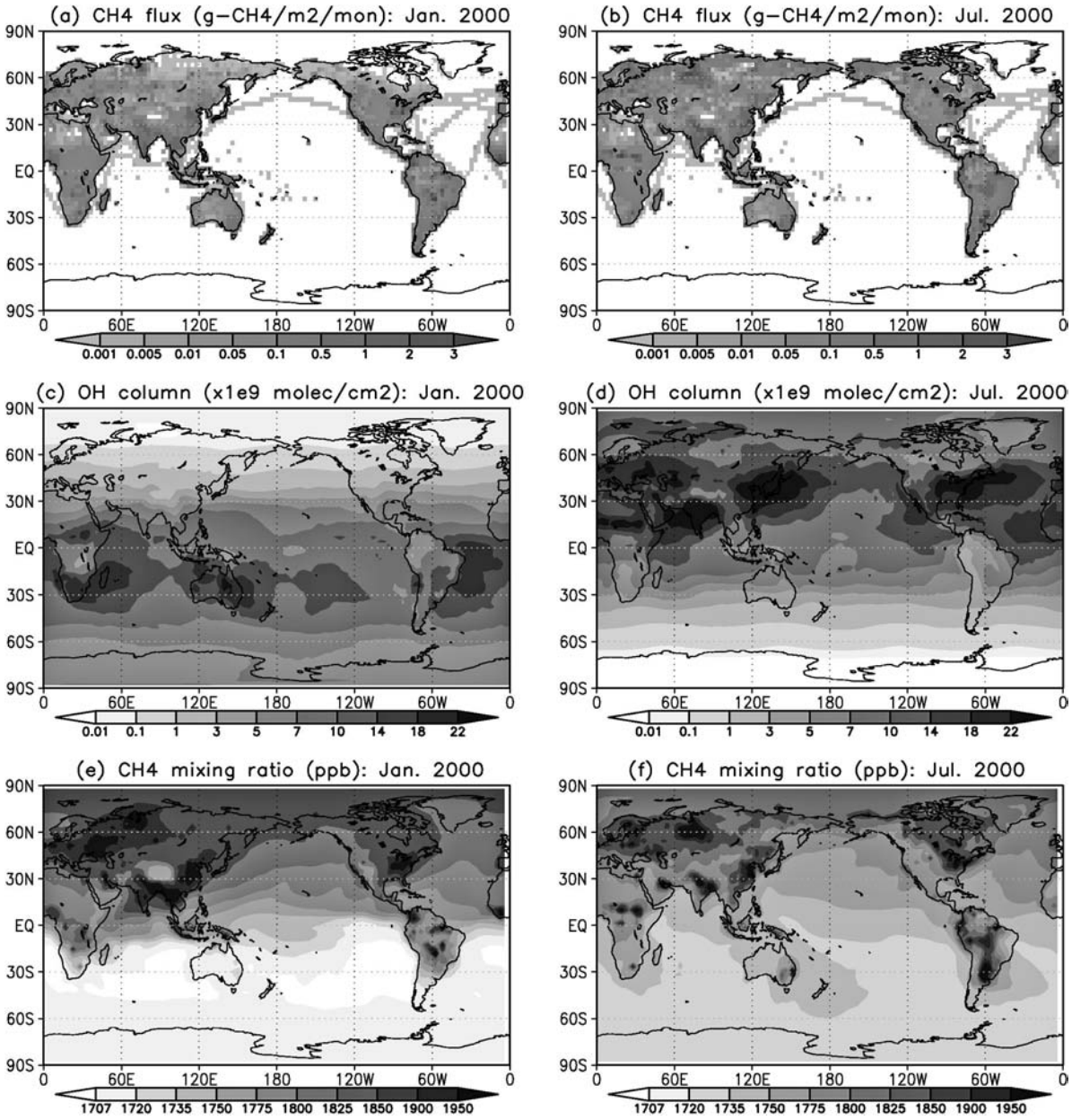

Fig. 1. Distribution of total CH_4 fluxes in January (a) and July (b) 2000 (top row), pressure-weighted columnar OH abundances during January (c) and July (d) climatology (middle row), and CH_4 mixing ratio at the earth's surface in January (e) and July (f) 2000 (bottom row) are shown at the ACTM horizontal grid resolution (T42). Values corresponding to each model grid are shown for the input (flux), and output (OH, CH_4) variables are depicted smoothed contour.

OH is assumed in this study (see Manning et al. 2005, for a debate on OH trends).

We have not accounted for the diurnal cycle in OH over the whole period of the simulation 1988–2006, which is known to exist in the observations near the surface (e.g., Kanaya et al. 2007). First two years of simulations is considered as model spin up for these fluxes (CH_4 initial condition is set from another 8 years of simulation) and not used in any of the analysis. A set of special simulations is made that includes diurnal variation in OH for the year 2002 only and the sensitivity of atmospheric

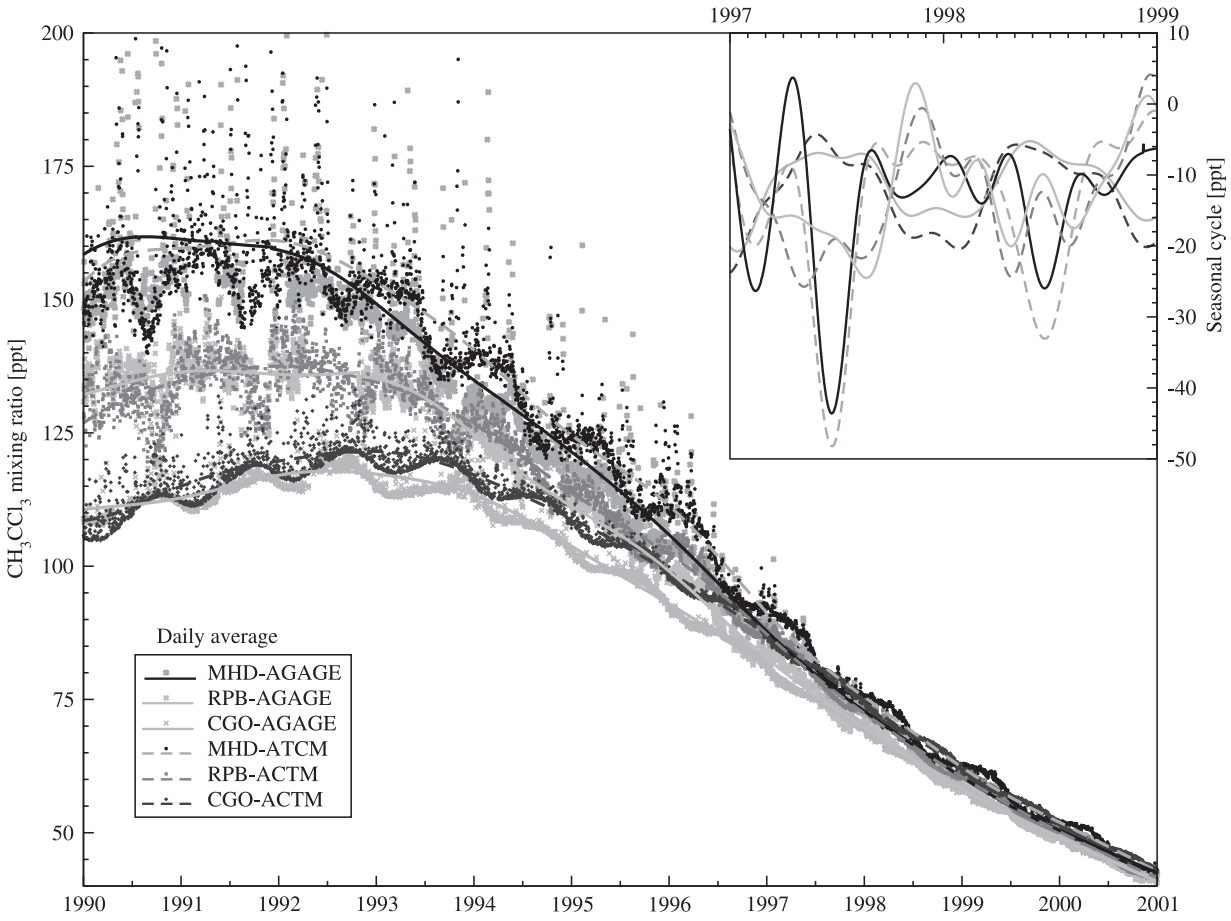

Fig. 2. Comparison of modeled and observed MCF timeseries at daily time intervals at 3 selected AGAGE monitoring sites, namely CGO, RPB and MHD (ref. Table 2 and Fig. 3 for site locations and abbreviations). These three sites are selected to show the latitudinal gradients in MCF as well as the distinct seasonal cycles and their variations with time and latitude. Solid lines are showing deseasonalised concentrations (i.e., the long-term trend component) and seasonal cycles (Inset; for the period of 1998–1999 only; = fitted curve − long-term trend) as derived using the digital filtering technique (ref. Section 2.3).

CH_4 to OH diurnal cycle is presented. For diurnally varying OH the CHASER full chemistry model output is sampled at hourly time interval. Later daily averages are calculated for the CH_4 simulation without diurnal OH because interpolating monthly-mean OH values (as used in control run) to model integration timestep would introduce extra bias in OH concentration.

2.3 Measurement network and data processing

Two types of CH_4 measurements, available from worldwide locations (see Fig. 3), are used in this study. Type 1 is based on flask sampling at several tens of sites and analysed at a central facility, mainly under the cooperative program organized by the NOAA Earth System Research Laboratory (ESRL, USA) as used in this study. Some observations are also available from other organizations, e.g., Commonwealth Scientific and Research Organization (CSIRO, Australia), National Institute of Water and Atmospheric Research (NIWA, New Zealand), Environment Canada (EC, Canada) (see Table 2 and WDCGG, 2007 for the full list). This set of sites is used for CH_4 growth rate analysis, based on the length of the measurement period being longer than ~1990–2006. Some unique flask sites (MKN in Kenya and BKT in Indonesia) are added to this growing measurement network in 2003 and are used only in seasonal cycle analysis. Type 2 are continuous measurements obtained

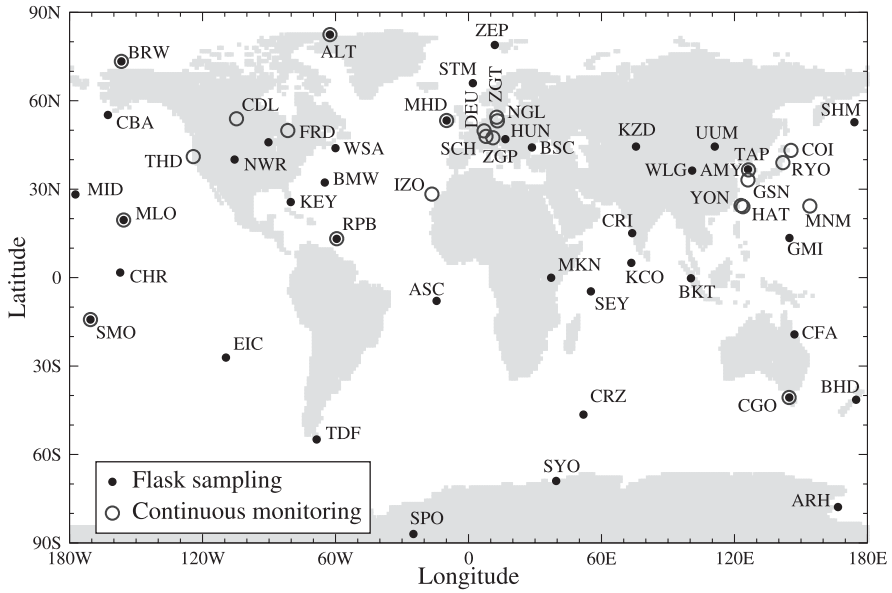

Fig. 3. Locations of measurement sites used in this work. Data from continuous monitoring sites are used for seasonal, synoptic and diurnal variation analyses, flask sampling sites are used for growth rate (those with longer record) and seasonal cycle analysis. The latitude and longitude for all sites and summary of statistics obtained by model-observation comparisons are given in Table 2. Following site abbreviations are used in this study (ordered alphabetically); ALT: Alert, AMY: Anmyeon-do; ARH: Arrival Heights, ASC: Ascension Island, BHD: Barring Head, BKT: Bukit Koto Tabang, BMW: Bermuda, BRW: Barrow, BSC: Black Sea, CBA: Cold Bay, CDL: Candle Lake, CFA: Cape Ferguson, CGO: Cage Grim, CHR: Christmas Island, COI: Cape Ochi-ishi, CRI: Cape Rama, CRZ: Crozet, DEU: Deuselbach, EIC: Easter Inland, FRD: Frasedale, GMI: Guam, GSN: Gosan, HAT: Hateruma, HUN: Hungary, IZO: Izaña, KCO: Kaashidhoo, KEY: Key Biscayne, KZD: Sary Taukum, MHD: Mace Head, MID: Sand Island, MKN: Mt. Kenya, MLO: Mauna Loa, MNM: Minamitorishima, NGL: Neuglobsow, NWR: Niowt Ridge, RPB: Ragged Point, RYO: Ryori, SCH: Schauinsland, SEY: Mahe Island, SHM: Shemya Island, SMO: Tutuila, SPO: South Pole, STM: Ocean Station "M", SYO: Syowa Station, TAP: Tae-ahn Peninsula, TDF: Tierra del Fuego, THD: Trinidad Head, UUM: Ulaan Uul, WLG: Mt. Walliguan, WSA: Sable Island, YON: Yonagunijima, ZEP: Zeppelinfjellet, ZGP: Zugspitze, ZGT: Zingst.

from in situ gas chromatographs, and this set of observations provide CH_4 timeseries at hourly intervals. This network is managed by the AGAGE network (USA, Australia, UK), EC, ESRL, Japan Meteorological Agency (JMA, Japan), Korea Meteorological Administration (KMA, Korea), Agencia Estatal de Meteorología (AEMET, Spain), National Institute for Environmental Studies (NIES, Japan), and Federal Environmental Agency (FEA, Germany) (WDCGG 2007). The continuous measurements are unique for analyzing synoptic variation and diurnal cycle in atmospheric-CH4.

The precision (1σ) of the high-frequency (continuous) measurements ranges between 1 ppb and 5 ppb, with a mean of about 3 ppb, with an added absolute calibration uncertainty of 1 ppb. The average precision for single flask measurements is assigned at about 5 ppb. While it is not crucial to incorporate accurate, absolute calibration scale for the analysis of CH_4 variability (growth rate, synoptic variability and diurnal cycle), all the measurements are required to be reported on a common absolute scale for the spatial gradients and seasonal cycle analyses. For uniformity all the observations are homogenized and shown on the Tohoku University (TU) scale (Aoki et al. 1992). The TU scale is in excellent agreement with the NOAA-2004 scale (Dlugokencky et al. 2005), and the latter has been accepted by the World Meteorological Organization (WMO) and Global Atmosphere Watch (GAW). We have multiplied the WDCGG reported CH4 values of AEMET, AGAGE, CSIRO, EC, ESRL, JMA, KMA, NIES, NIWA and UBA by 1.0121, 1.0, 1.0121, 0.9997, 0.9997, 0.9997,

Table 2. Pearson's moment correlation (r) statistics of the model-observation atmospheric CH_4 MR timeseries at all the sites considered in this study (first to last rows are ordered from North to South latitude), and number of data points (N) in each timeseries for correlations are given within parentheses as applicable. See the text for operating institutions full names, and Fig. 3 captions for site codes.

Abbreviated station name (Latitude, Longitude)	Model-observation timeseries correlation					Operating institution
	Growth Rate		Seasonal Cycle@ (2002–2005)	Synoptic Variability (2002–2005)	Monthly-avg. Diurnal Cycle (2002)	
	Control run (1992–2006)	FF Sensitivity (1998–2006)				
ALT (82°N,62°W)	0.23 (165)	0.84 (117)	0.90 (172)	0.35 (1058)	0.17 (275)	ESRL,EC
ZEP (79°N,12°E)			0.99 (207)			ESRL
BRW (71°N,156°W)	0.03 (165)	0.65 (117)	0.88 (184)	0.34 (1199)	−0.07 (288)	ESRL
STM (66°N,2°E)	0.42 (165)	0.81 (117)	0.98 (344)			ESRL
CBA (55°N,163°W)	−0.33 (165)	0.82 (117)	0.99 (366)			ESRL
ZGT (54°N,13°E)			0.50 (350)	0.60 (347)	0.29 (286)	UBA
CDL (54°N,105°W)			−0.57** (382)	0.21 (536)	0.73 (288)	EC
MHD (53°N,10°W)	0.53 (165)	0.24 (117)	0.92 (856)	0.61 (1307)	0.28 (287)	ESRL,AGAGE
NGL (53°N,13°E)			0.94 (770)	0.45 (1267)	0.91 (288)	UBA
SHM (53°N,174°E)	−0.22 (165)	0.82 (117)	0.81 (175)			ESRL
FRD (50°N,81°W)			0.51 (781)	0.36 (1252)	0.89 (287)	EC
DEU (50°N,7°E)			0.12* (352)	0.49 (854)	0.76 (288)	UBA
SCH (48°N,8°E)			0.77 (732)			UBA
ZGP (47°N,11°E)			0.39* (852)			UBA
HUN (47°N,17°E)			0.72 (152)			ESRL
KZD (44°N,76°E)			0.73 (144)			ESRL
UUM (44°N,111°E)			0.54 (190)			ESRL
BSC (44°N,29°E)	0.70 (127)	0.43 (117)	0.80 (114)			ESRL
WSA (44°N,60°W)			0.76 (113)			EC
COI (43°N,145°E)			0.94 (861)	0.56 (1284)	0.34 (288)	NIES
THD (41°N,124°W)			0.94 (851)	0.34 (1350)	0.24 (286)	AGAGE
NWR (40°N,106°W)	0.03 (165)	0.74 (117)	0.75 (227)			ESRL
RYO (39°N,142°E)			0.89 (835)	0.44 (1334)	−0.10 (286)	JMA
TAP (37°N,126°E)	0.25 (165)	0.66 (117)	0.78 (98)			ESRL
AMY (36°N,126°E)			0.34* (773)	0.22 (1176)	0.74 (288)	KMA
WLG (36°N,101°E)	0.17 (165)	0.11 (117)	0.59 (121)			ESRL
GSN (33°N,126°E)			0.68 (366)	0.20 (723)	0.22 (288)	KMA
BMW (32°N,65°W)			0.90 (116)			ESRL
IZO (28°N,16°W)			0.91 (483)	0.61 (959)	0.21 (288)	ESRL,AEMET
MID (28°N,117°W)	−0.09 (165)	0.52 (117)	0.85 (182)			ESRL

Table 2 (continued)

Abbreviated station name (Latitude, Longitude)	Model-observation timeseries correlation					Operating institution
	Growth Rate		Seasonal Cycle[@] (2002–2005)	Synoptic Variability (2002–2005)	Monthly-avg. Diurnal Cycle (2002)	
	Control run (1992–2006)	FF Sensitivity (1998–2006)				
KEY (26°N,80°W)			0.90 (147)			ESRL
YON (24°N,123°E)			0.95 (759)	0.52 (1223)	0.13 (287)	JMA
MNM (24°N,153°E)			0.98 (804)	0.51 (1294)	0.23 (286)	JMA
HAT (24°N,124°E)			0.96 (861)	0.69 (1218)	−0.01 (287)	NIES
MLO (19°N,155°W)	−0.04 (165)	0.57 (117)	0.90 (833)	0.55 (1305)	−0.13 (284)	ESRL
CRI (15°N,74°E)	0.29 (117)	0.66 (117)	0.73***			CSIRO
GMI (13°N,145°E)	0.85 (165)	0.04 (117)	0.82 (333)			ESRL
RPB (13°N,59°W)	0.53 (165)	0.42 (117)	0.92 (821)	0.60 (1251)	0.14 (281)	ESRL,AGAGE
KCO (5°N,73°E)			0.87***			ESRL
CHR (2°N,157°W)	0.76 (165)	0.50 (117)	0.53 (183)			ESRL
MKN (0°S,37°E)			0.73 (60)			ESRL
BKT (0°S,100°E)			0.87 (88)			ESRL
SEY (5°S,55°E)	0.32 (165)	0.57 (117)	0.84 (187)			ESRL
ASC (8°S,14°W)	0.47 (165)	0.54 (117)	1.00 (371)			ESRL
SMO (14°S,170°W)	0.69 (165)	0.59 (117)	0.96 (810)	0.48 (1190)	0.12 (276)	ESRL,AGAGE
CFA (19°S,147°E)			0.91 (77)			CSIRO
EIC (27°S,109°W)			0.86 (74)			ESRL
CGO (41°S,145°E)	0.66 (165)	0.70 (117)	0.99 (858)	0.63 (1350)	0.23 (286)	CSIRO,AGAGE
BHD (41°S,175°E)	0.35 (165)	0.74 (117)	0.77 (137)			NIWA
CRZ (46°S,52°E)			0.97 (165)			ESRL
TDF (55°S,68°W)			0.96 (44)			ESRL
SYO (69°S,40°E)	0.46 (165)	0.76 (117)	0.88 (96)			ESRL
ARH (78°S,167°E)	0.46 (160)	0.59 (113)	0.89 (36)			NIWA
SPO (90°S,25°W)	0.42 (165)	0.81 (117)	0.94 (226)			ESRL

[@] Fitted continuous data are used for seasonal cycle correlation calculation in the case both continuous and flask sampling are available for the sites. For the flask sampling sites original data (without fitting) as depicted in Fig. 7 are used, and thus an absolute difference greater than 60 ppb are excluded in calculating correlations for flask sampling sites.

* The low correlations results from weak (in comparison with the synoptic variations) and unclear CH_4 seasonal cycle at these sites. Large IAV in correlation coefficient are found at these sites; e.g., correlation between modeled and observed timeseries at AMY for 2002 or DEU for 2003–2004 are 0.66 and 0.56, respectively.

** The model failed to simulate high CH_4 concentrations during November–March season at this site.

*** Correlation at these sites is done for a different period (as in Fig. 8).

0.9997, 0.9967, 0.9977 and 0.9997, respectively, to convert all observations to the TU scale (based on Dlugokencky et al. 2005 and WDCGG 2007 reporting).

The model output is sampled at nearest model grid to the longitude, latitude and height of the measurement site. Due to the coarse horizontal resolution, the lower-most sigma-pressure model layer is flattened compared to the geographical terrain height and the surface model layer at the mountain sites are often located well below the site altitude. In this situation the model layer located just below the site altitude is selected. Processing of the timeseries to extract synoptic variations in CH_4 is identical to that has been done for CO_2 in Patra et al. (2008). A digital filtering technique is employed to fit the monthly or daily average timeseries to separate a signal representing seasonal cycle and long-term trends (Nakazawa et al. 1997). The fitted seasonal cycle is subtracted from daily average concentrations to calculate synoptic variability, and the growth rate is derived by taking time derivative of long-term trend component, separately for the modeled and observed timeseries. The diurnal cycle is extracted by subtracting daily averages from the hourly values corresponding to each day using unfiltered data. Pearson's moment correlation (r) and normalized standard deviation (NSD; = observed SD/modeled SD; 1σ) are used for evaluating similarity in the phase and amplitude, respectively, as appropriate for growth rate, seasonal cycle, synoptic variability and diurnal cycle between the simulated and observed timeseries. The atmospheric-CH_4 values are given in molar mixing ratio (herein after referred to as MR for brevity).

3. Results and discussion

Figure 1 shows the horizontal distribution of surface emissions (E2 scenario), column OH abundance, and CH_4 molar mixing ratio at surface during boreal winter and summer. The seasonality in emission distribution is contained in the biogenic or natural component of the emission, while the seasonality in OH field is mainly arising from seasonal variation in solar ultra violet (UV) radiation, water vapour and OH precursor species (ozone, nitrogen oxides etc.) as modeled in CHASER. Columnar OH shows greater concentrations over the continents and their outflow regions over the oceans, and the intensity is proportional to precursor gases concentrations (see for example Sudo et al. 2002), considering the UV radiation exposure is constant at a particular latitude band. Both CH_4 emission and OH loss has significant impact on controlling the seasonality in atmospheric CH_4 MR, which shows higher values in the Northern Hemisphere (NH) mid- and high latitudes during winter compared to the summer while the emission exhibits an opposite seasonal cycle. In the Southern Hemisphere (SH), lowest CH_4 MRs are simulated around 30°S in austral summer (January) compared to the winter. During the SH winter, CH_4 MRs decrease gradually with the increase in latitude from Equator to South Pole when the OH chemistry is relatively inactive. Thus OH is the most important factor in driving the atmospheric-CH_4 seasonal cycle in the mid- and high latitudes in both hemispheres. The seasonal changes in meteorology have maximum impact on CH_4 seasonality at the sites near the continental boundary, e.g., the ocean regions off the Asian coast during winter (Fig. 1e) show monotonically decreasing CH_4 MRs when the trade winds are from the land to ocean, but during the summer (Fig. 1f) when the trade winds are from ocean to land (under the influence of Asian monsoon circulation) sharp CH_4 changes are found at the continental boundary. More specific discussion is given with respect to model-observation comparisons of CH_4 MRs at some suitable sites shown in Fig. 3.

3.1 *Inter-hemispheric, latitudinal and longitudinal gradients*

Figure 4 shows the model-observations comparison of annual-mean CH_4 MRs at some regionally representative flask sampling sites operating for the period of this analysis (1990–2006). Generally, the ACTM simulations capture well the inter-hemispheric gradient and MR gradients between different latitude bands in the tropics, mid- and high latitudes of the two hemispheres. But the model failed to simulate the highest CH_4 MRs observed at the Black Sea (BSC) site in Romania for all the years. This underestimation of more than 100 ppb in modeled values is likely to be caused by missing some point sources of CH_4 near BSC in our course horizontal model resolution, and is excluded from the calculation of model-observation mismatch statistics. The Asian sites located over the high emission region (WLG, TAP) show greater CH_4 MRs compared to the background sites (away from the continent). The CH_4 MRs at NWR are fairly similar to the background CH_4 mixing ratio because this site is located away from the high

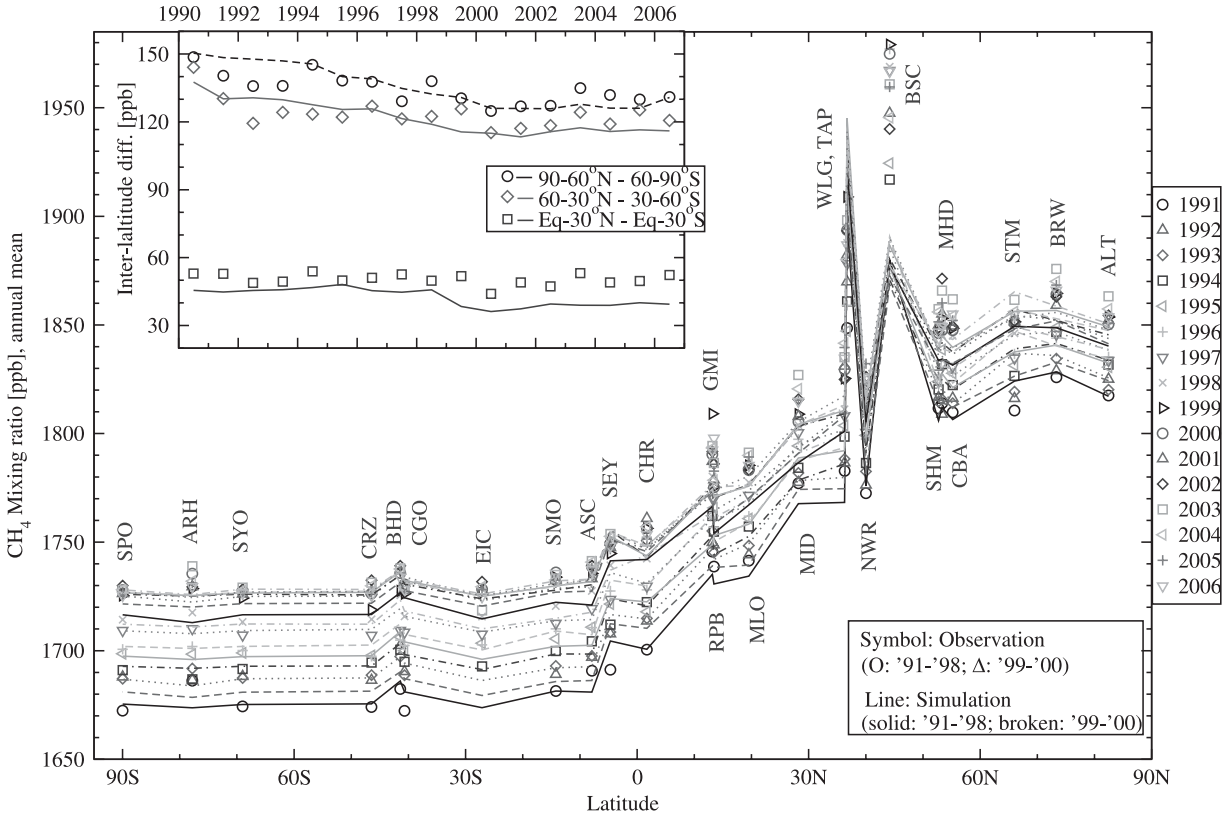

Fig. 4. Model-observation comparison of inter-hemispheric and latitudinal gradients and their interannual variability at some of the flask sampling sites. The north-south differences (inset; symbols—observations, lines—model) are deduced from observed and modeled annual mean mixing ratios (without BSC, due to extreme mismatch), after grouping the sites in two polar regions (60–90°S and 60–90°N), midlatitudes (30–60°S, 30–60°N) and tropical latitude (Eq-30°S, Eq-30°N) belts. All the observations are in TU scale.

emission regions in the eastern USA and the prevailing winds are from the west (ref. Fig. 1). Among the southern hemispheric sites, only ARH shows significant differences (~15 ppb) in observed and simulated annual means. Root mean square (RMS) differences between model-observation mismatches over all sites and for the period 1990–2006 are 13.6 ± 2.6 (1σ between years) ppb and 18.2 ± 3.0 ppb corresponding to the E2 and E1 emission scenarios, respectively.

The RMS statistics for the sites located in the latitude band of 5–60°N shows average differences between model-observation mismatches for different years are consistently lower by about 4 ppb for the E2 emission case (18.6 ± 4.2 ppb) compared to the E1 emission case (22.6 ± 3.9 ppb) in the period of 1990–2006. This comparison confirms suitability of the E2 emission scenario, compared to the E1 scenario, for CH_4 forward transport simulation using ACTM parameterized all transport and loss processes and set as the control case for this analysis. Major difference between the two emission scenarios can be seen in Table 1 (4 right columns), suggesting a large decrease in CH_4 emission from the Asian continent (India: 13 Tg-CH_4, China: 5 Tg-CH_4, Indonesia and Thailand: 3 Tg-CH_4) and an increase over the boreal regions (Russia and USA: 9 Tg-CH_4, Canada: 3 Tg-CH_4) on annual mean basis from E1 to E2 scenario. The source sectors due to rice cultivation and bogs are decreased while tundra and swamps are increased from E1 to E2 scenario (see Table 1 footnote). This regional emission balance to best match the longitudinal and latitudinal CH_4 MR gradients depend on the OH spatial distribution. For instance, if the integrated OH from CHASER model has greater NH to SH ratio compared to another model, the NH to SH CH_4 emission ratio has to be reduced (for

the other model) to obtained similar level of model-observation mismatches for inter-hemisphere gradients of CH_4 MR.

The average (over the sites falling in a particular latitude band) changes in inter-latitude gradients for the period of 1990–2006, between the poles (latitude: 60–90°), midlatitudes (latitude: 30–60°) and tropics (latitude: 0–30°) of two Hemispheres are shown in Fig. 4 (inset). During the period of our analysis, the differences between SH and NH latitude bands are generally well simulated by ACTM (systematic model-observation differences < 10 ppb). The prominent overestimation of NH-SH inter-polar differences by ACTM during 1991–1993 is likely to appear due to not accounting for reduction in Russian CH_4 emission in the early 1990s (see Dlugokency et al. 1998). This unaccounted Russian emission reduction, however, had almost no impact on the CH_4 MR differences between the two midlatitude regions (30–60°), and this comparison suggests that the reduced emission level persisted for only about 3 years. The temporal changes and IAV in ACTM simulated and observed inter-latitude differences agree well for the period 1990–2006. No significant change in model-observation differences between two tropical latitude bands are seen over the whole period of analysis, suggesting that the trends and variability in CH_4 emission or OH concentration varied similarly in the SH and NH tropical latitude bands at inter-annual timescale. The model tends to over predict (~9 ppb) the sudden drop in observed (~6 ppb) difference between SH and NH tropics around the 1998–2000 period, resulting in a greater systematic bias in modeled to observed inter-tropical difference.

In the SH mid- and high latitudes (south of 20°S), annual mean CH_4 MR differences between the sites are much smaller compared to the NH sites (Fig. 4). However, as seen from Fig. 1e some longitudinal differences are visible during the austral summer (January) around the 30–40°S latitude belt. Figure 5a shows model-observations comparison of the offsets in January-average CH_4 MR at Crozet Island (CRZ) and CGO with respect to Easter Island (EIC). We estimated the CH_4 MRs at CGO are consistently lower by 4.2 ± 1.5 (average $\pm 1\sigma$ interannual variability) and 6.0 ± 1.3 ppb with respect to EIC, corresponding to the observations and simulation, respectively. During January, the averages of observed and modeled offsets are estimated at CRZ with respect

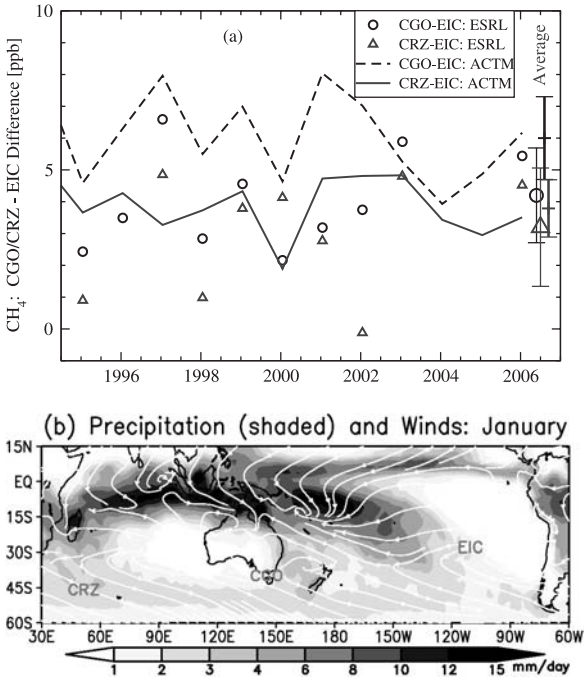

Fig. 5. (a) Timeseries and averages of offsets in CH_4 MR at CGO and CRZ sites with respect to EIC for the January-average values. The large symbols and vertical lines on the right are showing average $\pm 1\sigma$ differences over the period 1996–2006 for observed and modeled values, respectively. (b) January climatologies of the Climate Prediction Center (CPC)'s Merged Analysis of Precipitation (CMAP; source: www.cdc.noaa.gov, path: cdc/data.cmap.html) and NCEP/NCAR reanalyzed winds (source: www.cdc.noaa.gov, path: cdc/reanalysis/) streamlines are shown. The CGO, CRZ, EIC site locations are marked approximately.

to EIC are 3.2 ± 1.86 and 3.79 ± 0.9, respectively. The longitudinal difference in austral summer can be attributed to CH_4 chemical loss coupled with atmospheric transport, i.e., the North-South transport is more limited at EIC (East Pacific) than it is at CGO (West Pacific). This is due to the inclined shape of South Pacific Convergence Zone (SPCZ), centered at 5°S over the West Pacific (~150°E) and extending up to the Central Pacific (~140°W) with the center being located at 25°S (based on the analysis of precipitation and wind patterns; Fig. 5b). At the same time a weak Intertropical Convergence Zone (ITCZ) is located just north of the Equator

covering the Pacific Ocean. Such meteorological condition causes extra isolation dynamically around EIC (ref. Fig. 5b), resulting in one of the lowest CH_4 levels during the austral summer on the earth's surface (ref. Fig. 1e). An average bias of 2–3 ppb exists between the modeled and observed offsets for both EIC-CGO and CRZ-CGO, which is likely to be arising from site representation error due to course horizontal resolution of ACTM ($\sim 2.8 \times 2.8^{\circ}$) at CGO, located close to the strong CH_4 emission region in the southeastern Australia (see Fig. 1a,b). The other two sites (EIC and CRZ) being remote, the modeled and observed CH_4 MR differences (EIC–CRZ) of -3.75 and -3.79 ppb, respectively, are found to be in excellent agreement, where the site representation error is smaller compared to the coastal or continental sites (Patra et al. 2008).

3.2 Interannual variability and growth rate

Interannual variability in CH_4 MR can arise from changes in surface fluxes, OH abundance in response to the chemistry-climate-biosphere interaction, and IAV in atmospheric transport. Only the latter is modeled realistically in our simulations by using IAV meteorological drivers for ACTM transport, such as the horizontal winds and temperature from NCEP AMIP-2 reanalysis. Therefore the model-data mismatches in CH_4 IAVs can generally be attributed to surface flux and OH variability, assuming the model transport is an accurate representation of real atmospheric transport. Figure 6 shows the CH_4 IAVs at selected sites with long-term observations along with land surface temperature anomalies (Hansen et al. 2006) and satellite derived fire counts (Arino et al. 2005); the correlation statistics of model-observation comparisons are given in Table 2. At the boreal NH sites (ALT, BRW, CBA, MHD), the observed variability has slightly increased during 2000–2006 period ($1\sigma = 6.57$ ppb yr^{-1}) compared to the 1990–1996 ($1\sigma = 6.76$ ppb yr^{-1}), and this effect is also seen at the remote subtropical NH sites like MLO. Generally, the ACTM simulation fails to capture the observed IAVs at these sites during the 2000s, except the decrease in decadal average CH_4 growth rate, indicating the role of other parameters (presumably the fluxes and/or OH) than the transport IAV in controlling CH_4 growth rate over the Northern mid- and high latitudes regions. The surface land temperature anomaly stayed at a warmer level (average anomaly $+0.27^{\circ}$C) in the NH mid- and high latitudes during 2002–2006 period, compared to an average anomaly of $+0.04^{\circ}$C during 1990–1996 period (Fig. 6, top-left panel), which has been suggested as the main driver for wetland CH_4 emission variations at high latitudes (Walter et al. 2001).

On the contrary, at all SH sites (SEY, ASC, SMO, CGO, BHD, SYO, ARH, SPO) the amplitude of the variability in CH_4 growth rate has decreased significantly during 2000–2006 ($1\sigma = 2.32$ ppb yr^{-1}) compared to the previous decade ($1\sigma = 5.67$ ppb yr^{-1} for 1990–1996). At the moment, no causal relationship can be established and we suggest the reduction in inter-latitude difference led to smaller variability in NH to SH transport of CH_4. A surprising consistency in observed and modeled IAV as well as the decadal shift in CH_4 growth rate are found at all these sites, average growth rates of about 5.9 ± 7.0 (1σ) and 5.3 ± 2.6 ppb yr^{-1} in the 1990s to 0.0 ± 2.4 and 1.2 ± 2.0 ppb yr^{-1} during the period 2000–2006, respectively. The model-observation agreement is found to be the best at the tropical sites (GMI, RPB, CHR, SMO) and fairly well at some midlatitude sites (BSC, MHD, CGO), further emphasizing the role of transport in simulating CH_4 growth rate IAVs near the earth's surface. The interhemispheric transport time (IHTT) which shows largest variability near the equator (Patra et al. 2009) is probably the main driver for IAV in CH_4 growth rate at the tropical sites. The interhemispheric transport is leakier if the convection zones are weaker at the ITCZ and SPCZ, and the isolation of transport across the tropics is stronger when the convections are stronger. This result also implies a minor role for forest fires (natural biomass burning), shown in Fig. 6 (top-right panel), in reproducing the observed IAVs in CH_4 growth rate at the tropical and SH sites, except for the prominent mismatches observed during the 1997/1998 biomass burning period.

As a sensitivity study, we have simulated the interannually varying forest fires (FF) CH4 emissions (van der Werf et al. 2006) as a tracer during the period 1998–2006 when the forest fires emission estimates are available since the operation of ATSR satellite (Arino et al. 2005). The FF tracer run is setup in ACTM separately from the other CH4 emissions, but by employing the identical chemical loss processes and transport. The correlations of FF tracer with observed growth rate IAVs are given in Table 2 and depicted in Fig. 6 (thin line). While the maximum forest fire occurrences are

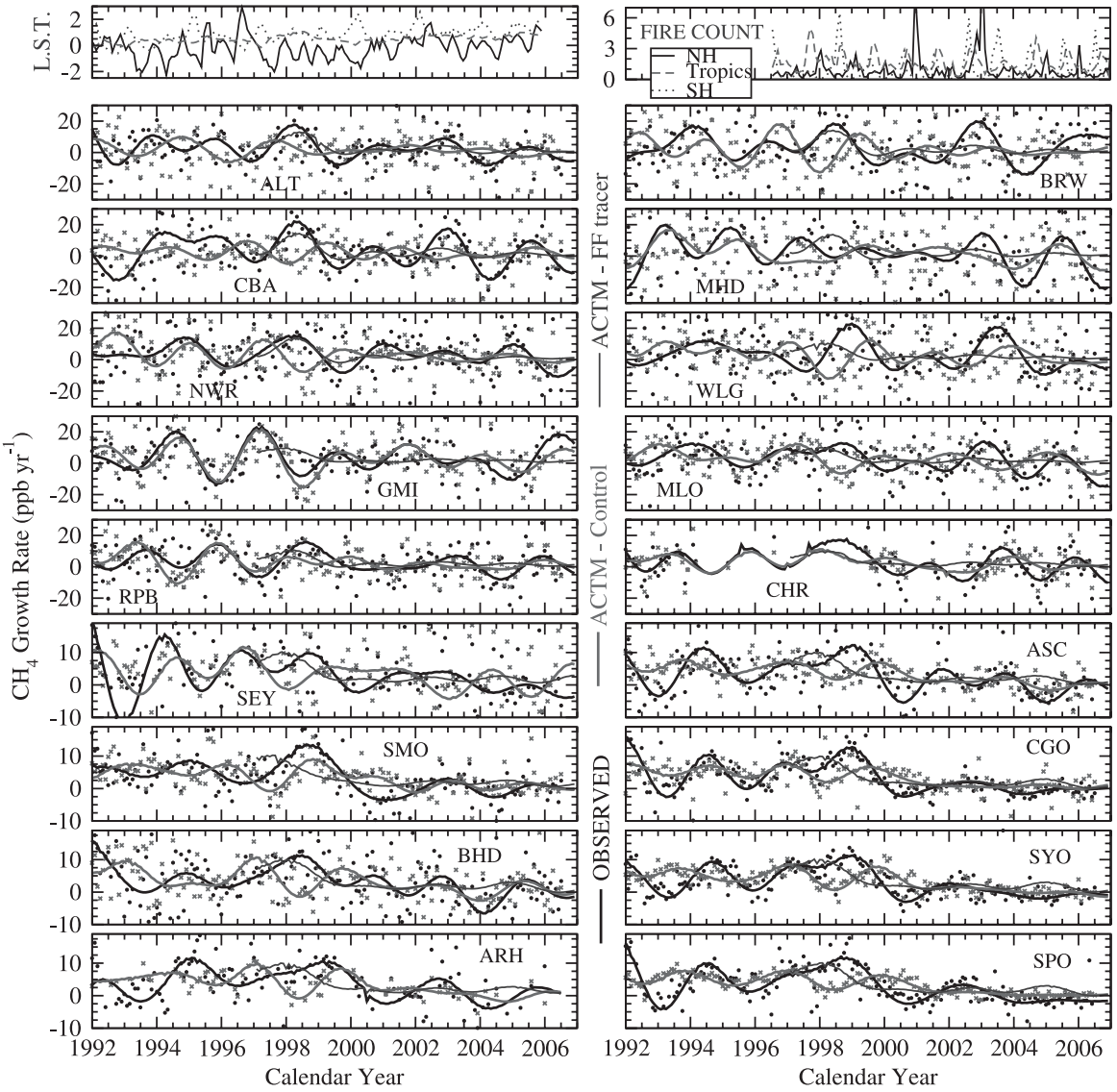

Fig. 6. Interannual variability in CH_4 growth rate and its changes in the period of 1992–2006 at selected stations covering most oceanic basins and latitudes (ref. Fig. 3 for site locations). The symbols and lines are the growth rates derived using monthly mean values before and after digital filtering, respectively, and thick dark, thick light and thin light lines correspond to observed, modeled and forest fire (FF) emission tracer. Top-left column is showing latitudinal average (SH: 90°S–30°S, Tropics: 30°S–30°N and NH: 30°N–90°N) land surface temperature (L. S. T.) anomaly relative to the average climatology over the period 1951–1980 (source: http://data.GISS.nasa.gov/gistemp). Top-right column is for Along Track Scanning Radiometer (ATSR) fire counts (source; http://dup.esrin.esa.int/ionia). The fire counts are normalized by long-term means corresponding to SH, Tropics and NH latitude band, by 193, 3148 and 2414, respectively for plotting on a common axis. Effect of temperature on wetland CH_4 emissions is not included in this study. Top panels legends are common.

found to be located in the tropics (top-right panel), higher correlations are generally obtained for the high latitude sites in both hemispheres and lower correlations for the tropical sites. Note that the correlations include both IAV and trends components in the CH_4 growth rates. The higher correlations are presumably because of the CH_4 build-up through the autumn and winter seasons after the

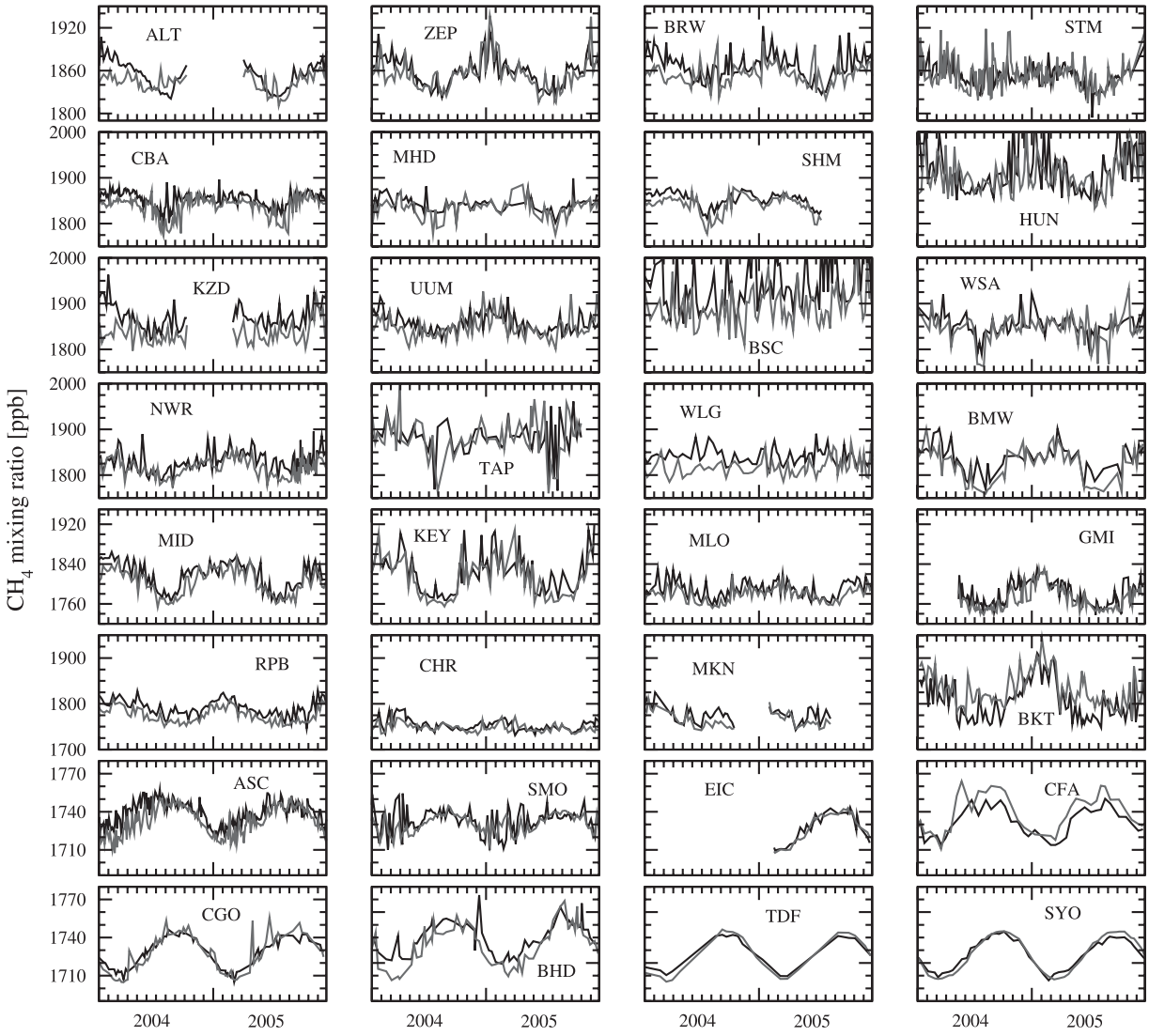

Fig. 7. Model (grey)–observation (black) comparison of seasonal cycles of CH_4 in the period of 2004–2005 at selected sites. Two full seasonal cycles are shown to depict that model-observation agreement differ from one year to another significantly and to include at least one full seasonal cycle for all sites due to missing data. For the correlations in Table 2 data for 4-years period are used (2002–2005). All the observations have been converted to the TU scale.

major forest fires during the summer in the high latitude region.

3.3 Seasonal cycles and evaluation of surface fluxes

Figure 7 shows the comparison of modeled and observed seasonal cycles at selected sites distributed around the world and the correlation statistics are given for additional sites in Table 2. The correlations are calculated over the period of 2002–2005 when CH4 MR growth rates are close to zero, and depicted in Fig. 7 for two years period of 2004–2005 because some sites have data gaps over a few months in a particular year. At all sites, the ACTM simulations are able to capture salient features in the observed seasonal cycles (average correlation 0.78; range: 0.12–1.0). In the correlation calculation, model-observation differences greater than 60 ppb are rejected to avoid large spikes in the observed timeseries lasting only one time-point at

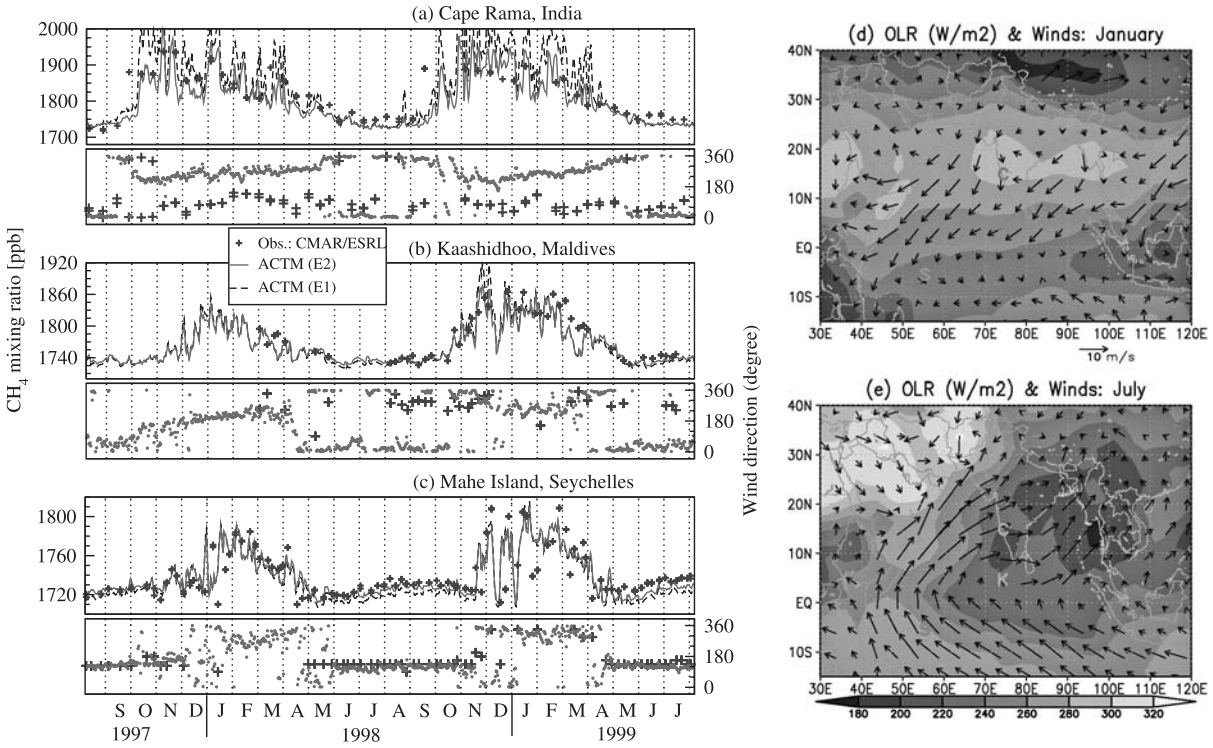

Fig. 8. Comparison of ACTM simulations (for both E1:broken line and E2:solid line emission scenarios) and observations (symbols) of CH_4 MRs at three sites near the Indian subcontinent, (a) Cape Rama (CRI), India, (b) Kaashidhoo (KCO), Maldives, and (c) Mahe Island, Seychelles (SEY). Modeled (line) and observed (symbol) wind directions are plotted in the bottom panels. The match between the model and observation at CRI is inferior during November–December 1998 compared to the year 1997. Tickmarks are placed at one month time intervals on the x-axis. On the right column monthly-mean, averaged over 1996–1998, outgoing longwave radiation (OLR in W m^{-2}; shaded) and wind vectors (in m s^{-1}, see legend) are depicted for two distinct seasons in the Indian subcontinent; showing continental outflow during north-east monsoon (d; boreal winter) and south-west monsoon bringing clean marine air from the SH Indian Ocean to these sites (e; boreal summer). The site locations are marked by S, K and C in red for SEY, KCO and CRI, respectively. All the observations are in TU scale.

some sites (e.g., MHD). This rejection limit is reasonable, considering that the differences between annual mean model-observation differences are typically smaller than 25 ppb (ref. Section 3.1). The high correlations are obtained due to realistic representation of (a) interhemispheric transport times in ACTM (see Patra et al. 2009, for further details) and the CH_4 latitudinal gradient, (b) monthly variations of regional scale distributions of CH_4 fluxes and chemical loss parameterization in the troposphere and stratosphere, and (c) seasonal/synoptic changes in trade winds due to nudged meteorology.

The role of emissions and seasonal transport changes in simulating CH_4 seasonal cycle can be better visualized by focusing this comparison on a few adjacent sites at once. As an example, here we show (Fig. 8) the CH_4 seasonal cycles at CRI (India), KCO (Maldives) and SEY (Seychelles) stations to evaluate the emission distribution over the Indian subcontinent for both emission scenarios. As shown by the boreal winter (January) and summer (July) time meteorological conditions (Fig. 8d,e), these sites are under the influence of the north-east and south-west monsoons, respectively, when a high and low pressure system is located over India as indicated by more (clear sky) and less (cloudy sky) outgoing long-wave radiation (OLR). During January, the CRI site is observing air mass directly from India, before any significant chemical loss of CH_4 could occur, which is one of the CH_4 emission hotspots due to large livestock population and rice cultivation (Yamaji et al. 2003; Yan et al. 2008). How-

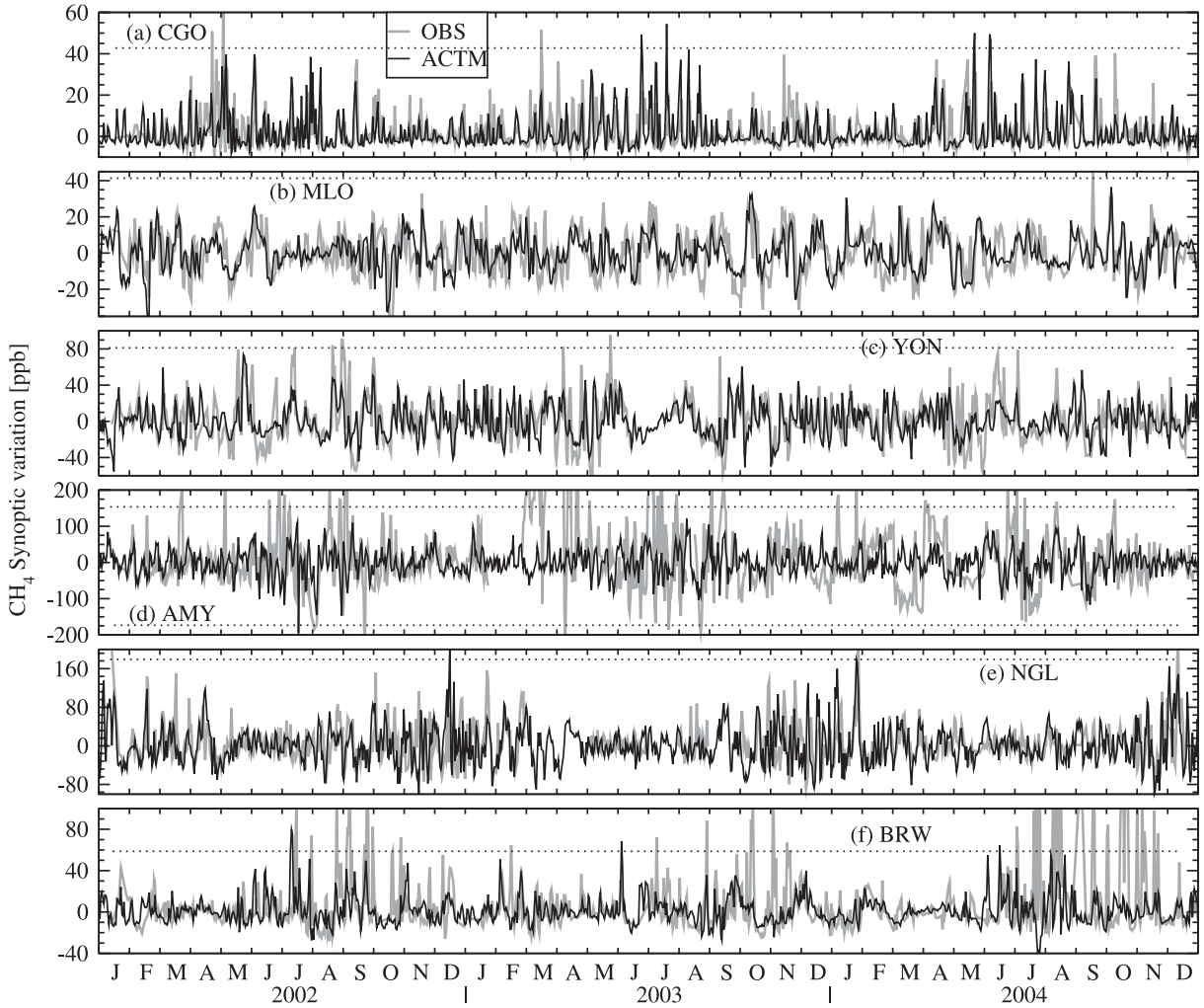

Fig. 9. Examples of CH_4 synoptic variations, obtained by subtracting the fitted seasonal cycle from daily-averaged CH_4 timeseries (dark line: model, grey line: observed), separately for the model and observation. The dotted horizontal line is drawn at 4.5σ for each timeseries and used as the cutoff level for data to be included in correlation calculation (see text). Panels are organized by site location, from south (CGO; top-left) to north (BRW; bottom-right) latitude. Only the observation gaps longer than 4 days are seen as discontinuity in line.

ever, an annual total emission of 54 Tg-CH_4 yr^{-1} (Fig. 8a; E1 scenario; represented by broken line) is greater than required for a successful simulation of observed CH_4 seasonal cycle and amplitude of fluctuations present in bi-weekly observations at CRI (symbols). The ACTM simulations using E2 scenario having annual total emission of 41 Tg-CH_4 yr^{-1} is closer to the observed value (red line), particularly during the October-March months. The Indian emission signal in atmospheric CH_4 quickly drops by tens of ppb and ~100 ppb for the peak values in seasonal cycles at KCO and SEY, separated by approximately 10° and 20° latitudes from CRI, respectively. Large weekly scale CH_4 variability is observed at SEY site during December–January due to quick reversal of wind direction (Fig. 8c, bottom panel). SEY is located within the intertropical convergence zone (ITCZ), seen as the cloud band (grey colour in Fig. 8d), which separates the CH_4 rich NH air from CH_4 depleted SH air. We conclude that accurate simulations of interhemispheric concentration gradients are necessary for better agreement between modeled and observed seasonal and synoptic variations

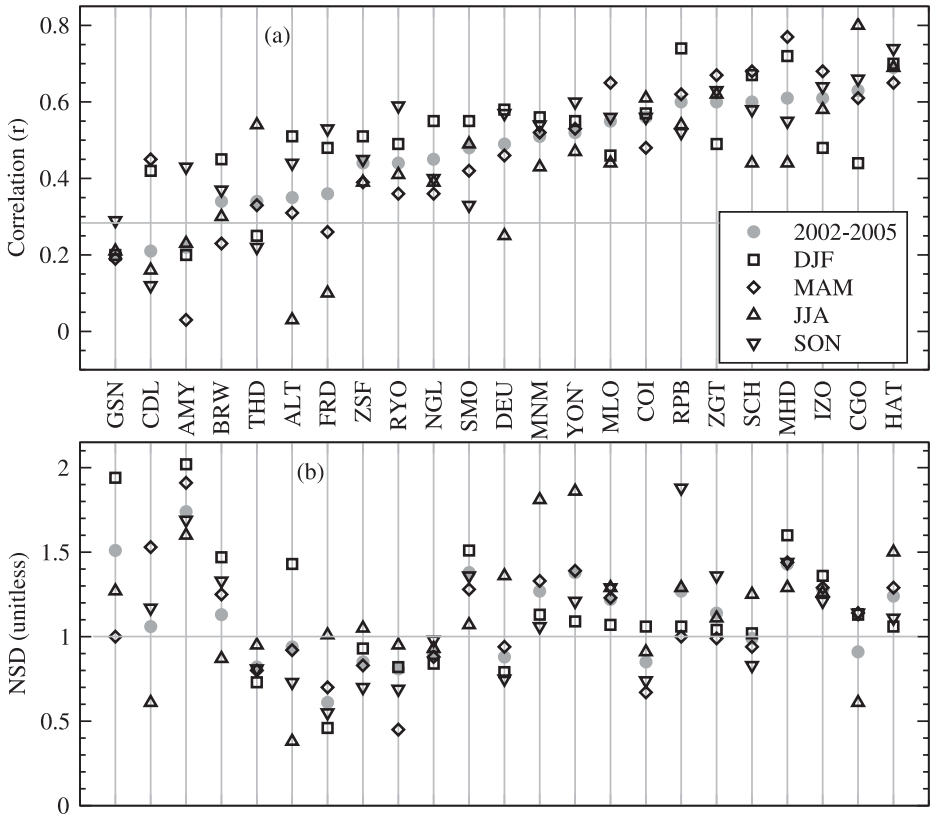

Fig. 10. (a) Correlations and (b) normalized standard deviations (NSDs) for CH_4 synoptic variations at each site for the 4-year period (2002–2005), and 4 seasons (DJF: December-January-February, MAM: March-April-May, JJA: June-July-August, SON: September-October-November) corresponding to each site. The sites on x-axis are ordered from lowest to highest correlation corresponding to 2002–2005 case in panel a. The 99% confidence interval for the correlation coefficient and NSD value of 1.0 (indicating perfect match between and modeled and observed variabilities) are marked by the grey lines in top and bottom panels, respectively.

in CH_4 at the tropical sites. This conclusion can be generalized as gradients in CH_4 MR distribution at regional scales around all sites have large implications for the simulations of CH_4 synoptic variability, and this is the focus of our discussion below.

3.4 Synoptic variations in daily average CH_4

Synoptic variations in CH_4 timeseries are described as the deviations of daily average values from a digital-filter fitted seasonal cycle (ref. section 2.3). Figure 9 shows the examples of synoptic variations as obtained by measurements and ACTM simulation at six selected sites. The observed and modeled variability are compared using correlations (r) and normalized standard deviations (NSDs) for phase and amplitude of the variability, respectively, and are depicted in Fig. 10 for all sites with continuous CH_4 measurements (WDCGG, 2007). This analysis is similar to that employed by Patra et al. (2008) for CO_2 synoptic variations. The only difference is that we have set a cutoff value of $\pm 4.5\sigma$ modeled variability for the observed CH_4 variations each site to calculate correlation and NSD, marked as the horizontal lines in Fig. 9. Synoptic variation in CH_4 is produced by the interaction between changes in synoptic weather, e.g., frontal flows, low or high pressure systems, and the contrast in regional distribution of CH_4 MRs (predominantly controlled by regional emission distributions), both extending about 1000×1000 km^2 spatial scales. Because the ACTM transport is nudged towards NCEP AMIP-2 horizontal winds at every 6-hourly interval, we assume a fairly accurate tracking of synoptic meteorology, such as the

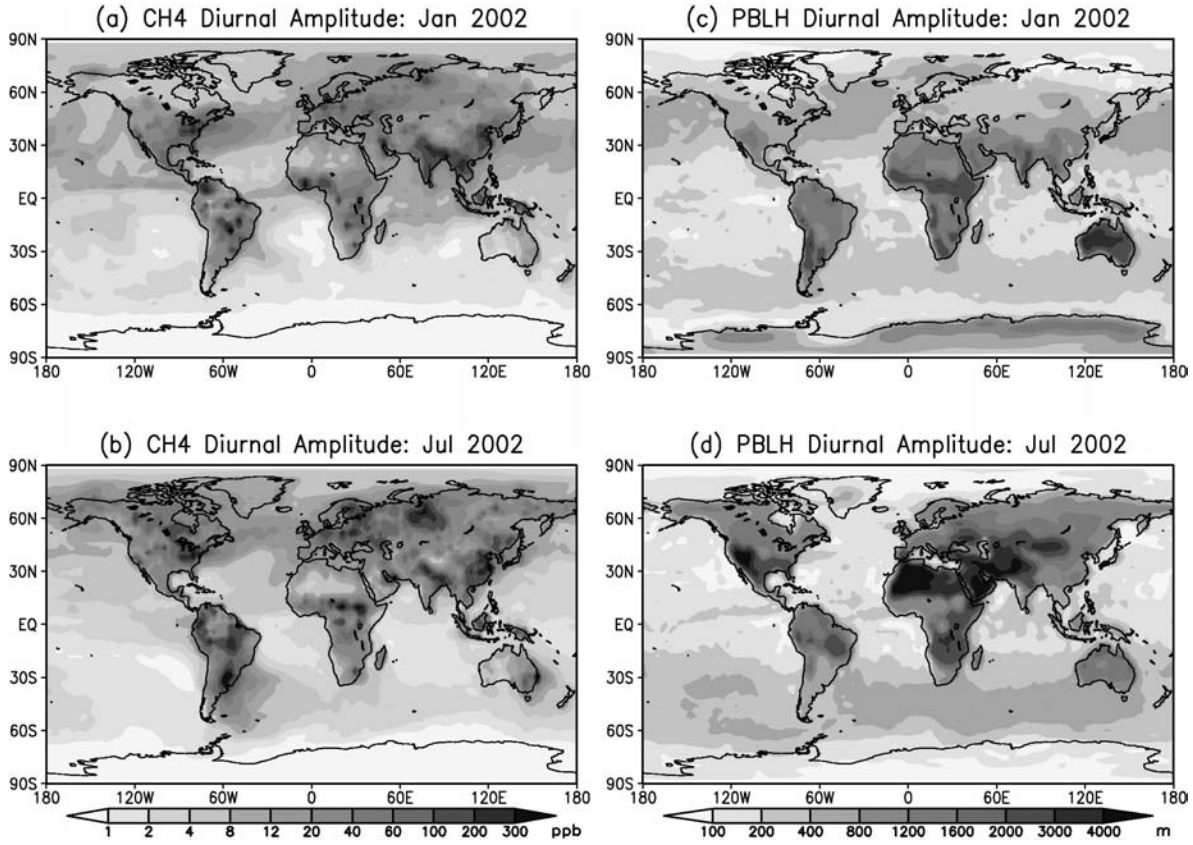

Fig. 11. Latitude-longitude distribution of model-derived monthly-mean diurnal cycle amplitudes of CH_4 at surface (left column) and planetary boundary layer height (PBLH; right column) in January and July 2002 (top row). The difference between maximum and minimum values in hourly ACTM output within a day at each model grid is defined as diurnal amplitude.

development and progress of synoptic systems in the model transport. Thus a reasonable distribution of surface emissions would produce statistically significant correlations and NSDs close to 1, which is evident from Fig. 9 and valid for most of the sites. At Amyeon-do (AMY) site, maximum synoptic variabilities are found during the boreal summer, when the Asian monsoon is in active phase and emissions over the Asian continent are at their seasonal high. For the midlatitude sites, the period of maximum variability coincides with the period of maximum frontal activity (e.g., May-Jun-Jul for CGO, Dec-Jan-Feb for NGL).

Only 3 out of 23 sites showed lower correlation than the line of 99% confidence interval in two-tailed Students-T significance test (Fig. 10 and Table 2). The CDL site has one of the shortest timeseries (540 daily-average data in the period Jan 2002–Dec 2005) with large spikes. Due to ACTM's coarse horizontal resolution ($\sim 2.8 \times 2.8^{\circ}$), it is unlikely to account for any large point sources affecting CH_4 synoptic variability. At AMY and GSN sites, the separation of seasonal cycle from the daily-average timeseries was not very clean (not shown) due to much greater synoptic variations in comparison with the seasonal cycle amplitude. In addition, sometimes data gaps are present for long periods, such as those seen at AMY during 2003 and 2004 (Fig. 9d). If we use the model-observation CH_4 synoptic variability only for the period of 2002, when there are no significant data gaps at AMY, the correlation increased to 0.32 and NSD is decreased to 1.28 from those depicted in Fig. 10. This suggests that careful selection of model and observation data can lead to improved comparison statistics. For example, ACTM's course horizontal resolution may not be sufficient to properly represent the synoptic meteorology and emission pattern

observed around the AMY site, but such site representation error (see Patra et al. 2008) can be reduced significantly by employing higher resolution in transport models without improving the meteorological drivers (Maksyutov et al. 2008).

Except at a few sites, the correlations or NSDs do not show significant seasonality that can be seen as the difference between the open symbols and the filled symbol. This contrasts what has been discussed for CO_2 (Patra et al. 2008), specifically, for the MLO site (correlation and NSD of ~0.13 and 2.8 for ACTM T42 version; named as CCSR_NIES1.FRGCG model). The correlation coefficient and NSD for observed and modeled CH_4 synoptic variability are found to be 0.55 and 1.24 at MLO. The better performance of ACTM for CH_4 synoptic variation than that of CO_2 can be assigned to a more realistic surface flux distribution of CH_4 over the Asian and North American continents that are transported to MLO compared to CO_2. The strong diurnal variations and existence of both positive and negative values in CO_2 flux, in contrast with positive values only for CH_4 flux, might also complicate the transport mechanisms for atmospheric CO_2. Furthermore, CH_4 has no significant flux over the remote ocean area, which is not the case for CO_2. Also, the diurnal transport patterns are not well captured at sites located on isolated mountains at altitudes well above the synoptic-scale PBL (e.g. IZO, and MLO) in framework of coarse ACTM horizontal resolution. Two other sites (CGO and ZGT) showed significantly lower correlations for CO_2 compared to CH_4 synoptic variability, and correlation differences at all sites are found to be within 0.15. These differences between CH_4 and CO_2 forward transport simulations suggest that transport modeling error may not be attributed correctly by CO_2 simulation alone. As discussed earlier the development of spatial gradients around the measurement location are important for realistically capturing the seasonal cycle and synoptic variation of the chemical species.

3.5 *Analysis of CH_4 Diurnal cycle and role of OH diurnal cycle on CH_4 simulation*

The variations in ACTM simulated planetary boundary layer height (PBLH) and CH_4 diurnal amplitude show good correspondence over the land and ocean during the winter and summer seasons (Fig. 11). In the finer scale (see Table 2), the diurnal transport patterns are not very well captured at coastal sites where the seacoast is not well defined

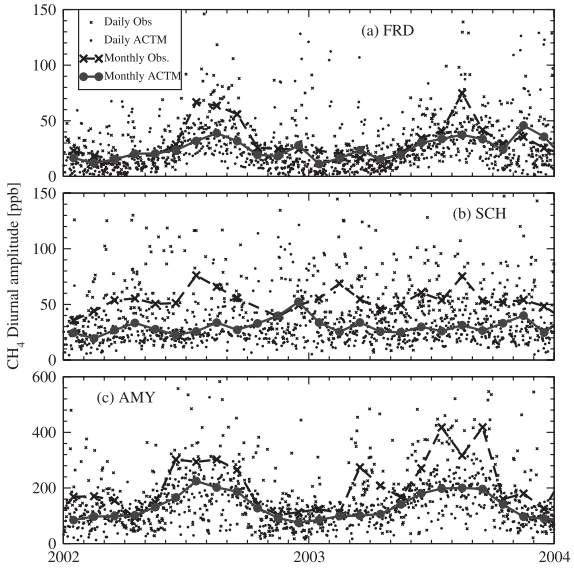

Fig. 12. Variations in observed (brown symbols and broken line) and ACTM simulated (light blue symbols and blue lines) diurnal amplitude in CH_4 MRs shown at three selected land sites, (a) Fraserdale (FRD), Schauinsland (SCH) and Amyeondo (AMY). Small symbols correspond to daily diurnal amplitude and the lines are for monthly-mean diurnal amplitudes.

in this transport model runs at coarse horizontal resolution (T42). Thus the diurnal changes in the land-see breeze and the resulting diurnal changes in CH_4 MR are not well simulated at the coastal sites, such as RYO (Table 2). At the continental sites, the average diurnal amplitudes and its seasonality (summer maxima) in CH_4 MRs can be reproduced fairly satisfactorily (Fig. 12). The underestimation at SCH is primarily due to coarse vertical resolution in ACTM; by selecting the next lower model level (#2) a factor of two increase in the diurnal amplitude can be achieved. Selection of the lower model level does not affect the model-observation comparison of synoptic variations, suggesting interpolation between model level #2 and #3 would produce optimized agreement between the model results and observations. There are no significant phase mismatches (not shown) in the CH4 diurnal cycle since the diurnal cycle appears to be solely caused by the PBLH diurnal variation, unlike that has been observed for the case of CO_2 (Law et al. 2008). The development of the CO_2 diurnal cycle is due to diurnal changes in photosyn-

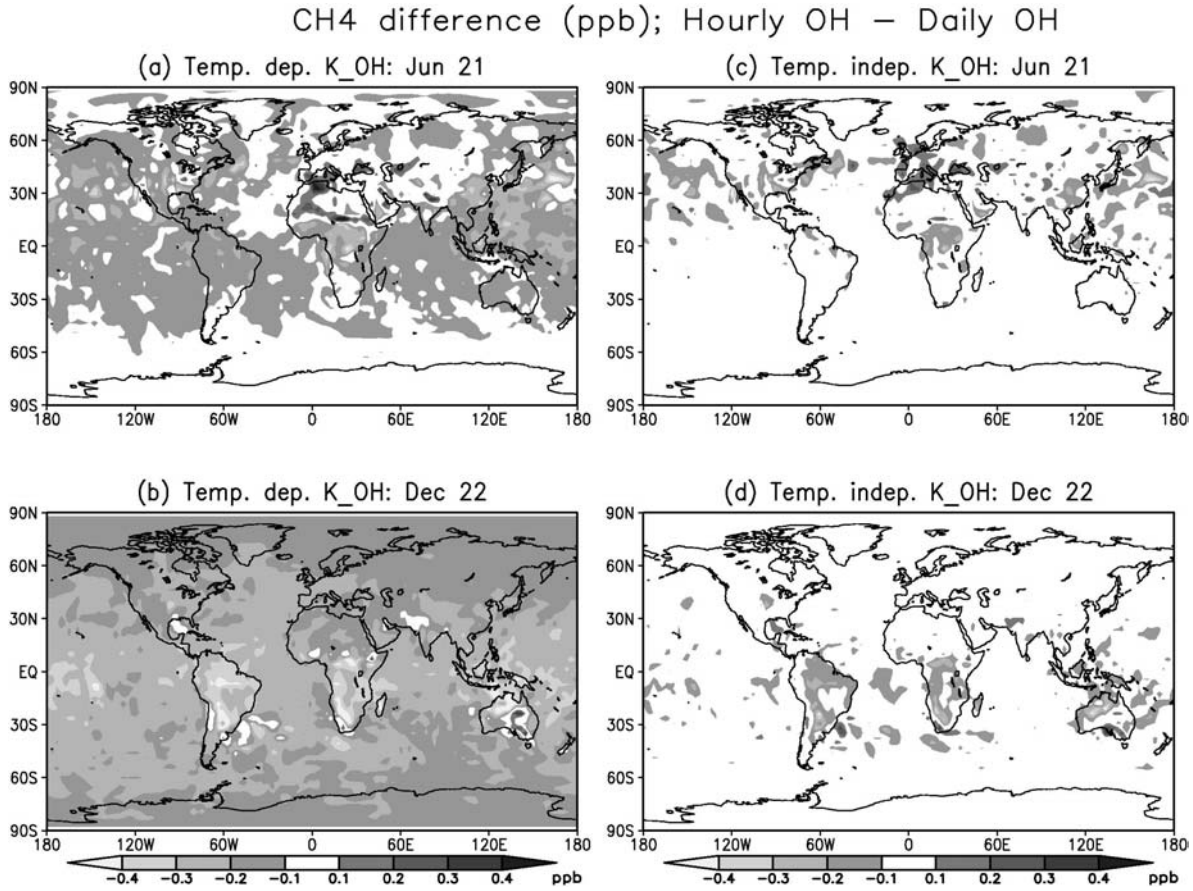

Fig. 13. Horizontal distribution of differences in ACTM simulated daily-average CH_4 at the surface using hourly-average and daily-average OH concentrations for June (top row) and December (bottom row) Solstice days of 2002. The results on the left (right) column correspond to the simulation by including (excluding) temperature dependent reaction rate of CH_4 with OH (K_{OH}). Note these sensitivity simulations are started from 1 Jan 2002, 00UT with identical initial conditions, provided by the control run that uses monthly-mean OH concentrations.

thetic uptake during the day and PBLH variation.

So far we have discussed CH_4 forward transport simulations using climatological monthly mean OH concentration. Here we evaluate the role of diurnally varying OH in simulating CH_4 cases for one year (2002). The CHASER full chemistry model output of OH is sampled at hourly time intervals, and daily average OH concentrations are constructed from these hourly values for this sensitivity analysis. Differences in CH_4 MRs due to the use of hourly and daily average OH concentrations in ACTM simulations are shown in Fig. 13 (mostly less than 0.4 ppb). This indicates that accounting for OH diurnal cycle is not crucial for simulating diurnal, synoptic and seasonal variations in CH_4 MR, and suggests that the CH_4 chemical lifetime in the troposphere is longer than that due to atmospheric transport (discussed further in the next section). However, the spatially-averaged CH_4 values are found to be smaller by about 0.2 ppb for the simulation case that used hourly OH concentrations in comparison with daily OH concentration in December, after about one year of model integration. This negative bias in CH_4 MRs (Fig. 13a,b) is simulated mainly because of the temperature dependence of K_{OH}. Even though the total OH radical number is identical over a one day period, the OH concentrations are much higher during the day in the case of hourly OH field, coinciding with the higher air temperature during the day than in

the night (typical temperature rise in the morning lags OH increase by a few hours; see Kanaya et al. 2007). For example, an increase of 10° (from 290 K to 300 K) in air temperature will raise the K_{OH} by 23% (from 5.38×10^{-15} to 6.60×10^{-15}). Since the diurnal variations in temperature are greater over the land regions, the maximum differences between two simulations using hourly and daily OH concentrations appear larger on land surfaces or over the ocean regions adjacent to large continents (Fig. 13). To confirm this other simulation with fixed temperature for K_{OH} calculation at 290 K has been conducted; no apparent negative bias persists if global average CH_4 MR differences are considered over the 1 year simulation period (Fig. 13c,d). A difference of 0.2 ppb in global average CH_4 MR would disturb the CH_4 budget by less than 1 Tg-CH_4 on an annual basis.

3.6 *CH_4 budget in the troposphere*

A balance between CH_4 emission at the earth's surface and chemical loss in the troposphere (plus escape to the stratosphere) is required to maintain the modeled tropospheric growth rate in close agreement with the observation. Table 1 shows budget of CH_4 emission, atmospheric burden and sink amounts for the year 2000, yielding an atmospheric lifetime of 8.62 years (= 4999 Tg-CH_4/580 Tg-CH_4 yr^{-1}; ratio of burden to sink). This CH_4 lifetime is in good agreement with the mulimodel mean lifetime of 8.7 ± 1.3 years estimated using 26 state-of-the-art CTMs (Stevenson et al. 2006). The total CH_4 sink exceeds the net emission by ~5 Tg-CH_4 yr^{-1}, suggesting an overall negative growth rate for the year 2000. This can be confirmed by the model-observation growth rate comparison shown in Fig. 6. The amount of imbalance between emission and sink for the year 2000 (5 Tg-CH_4) is consistent with the global increase rate of −1.6 ppb/yr estimated using the observed time-series. What drove such a large increase in the CH_4 sink is not obvious. However, our model simulations suggest vertical transport differs significantly from year to year, and, coupled with horizontal transport, can cause large differences in CH_4 MRs at different altitudes. A faster transport of CH_4 from the surface will effectively reduce CH_4 MRs at the most measurement sites considered here. The role of OH variability in driving CH_4 loss seems weak, because instantaneous CH_4 chemical lifetimes (see Fig. 14) are several orders of magnitude longer compared to the dynamical

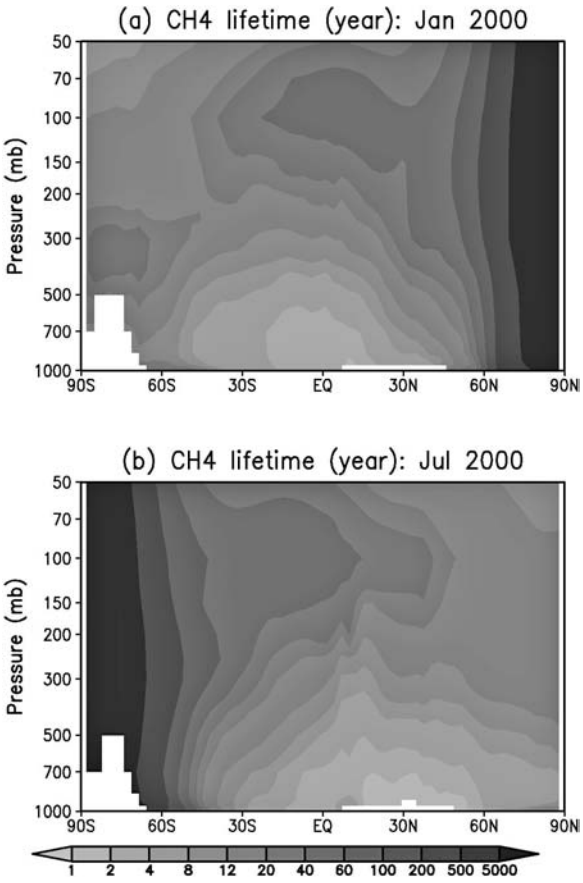

Fig. 14. Latitude-pressure distribution of monthly-average instantaneous CH_4 lifetime ($= 1.0/[K_{O^1D} \times O^1D + K_{OH} \times OH + K_{Cl} \times Cl]$) at model grids during (a) boreal winter and (b) boreal summer of 2000.

residence times at regional-hemispheric scales (~week to months). The lower (higher) CH_4 concentration in the surface model layer can result from faster (slower) vertical transport between different model layers, followed by the horizontal transport. Thus it is proposed that large part of CH_4 growth rate IAVs near the earth's surface are likely to arise from atmospheric dynamics (and fluxes at the NH high latitudes) as discussed earlier.

Because a large part of IAV in CH_4 growth rate variability near the earth's surface is arising from atmospheric transport, some of the IAVs in surface CH_4 MR may not represent a net increase in atmospheric CH_4 burden. To illustrate further, Fig. 15 shows the vertical and horizontal cross-sections of model simulated difference in CH_4 between two adjacent years, 2003 and 2004, for the month of July.

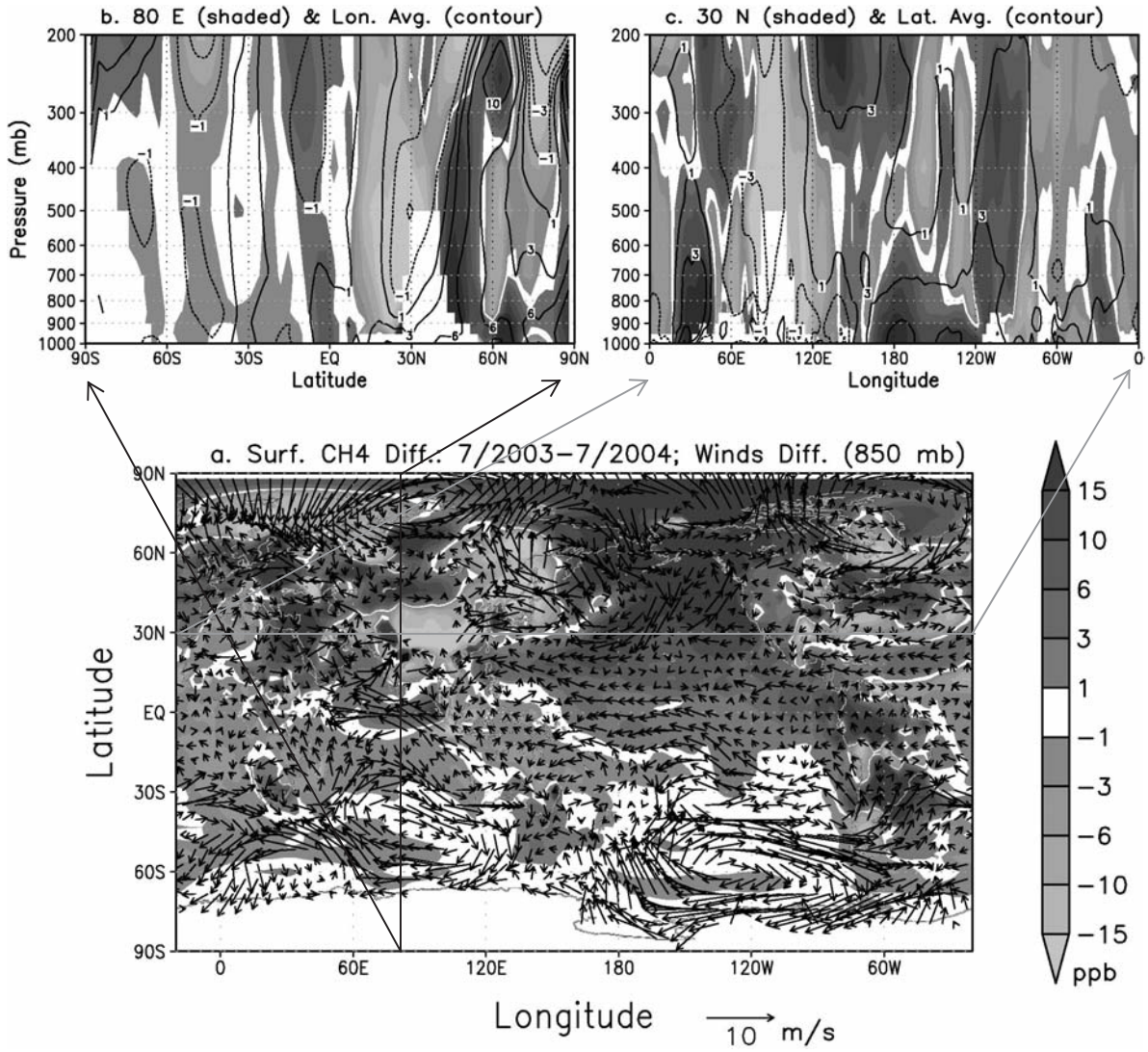

Fig. 15. Latitude-longitude distribution of differences in monthly-mean CH_4 MR at the earth's surface and wind vectors at 850 mb height between 2003 and 2004 in July are shown (a; bottom). Latitude-pressure (b; top left) and longitude-pressure (c; top right) vertical cross-sections are shown for CH_4 MRs only, for a particular longitude (80°E and longitudinal average 0–360°E) and latitude (30°N and latitudinal average 90°S–90°N), respectively, as indicated by the black and grey lines. Note that the longitudinal (latitudinal) average values are up to a factor of 10 smaller than those at particular longitude (latitude) and the difference between years reduced further for the global averages (see text).

The CH_4 growth rates at some of the surface sites in 2003 were as high as those observed in 2007, but no net increase in emission is suggested for 2003 when IAV in OH concentration is included (Rigby et al. 2008). Figure 15 suggests that the Indian monsoon was stronger in July 2003 compared to the July 2004 (seen as intensified south-westerly winds over the northern Arabian Sea), and lifted CH_4-rich air from the surface over the Indian subcontinent to the upper troposphere by deep cumulus convection. The east-Asian monsoon winds were also stronger in July 2003 compared to July 2004. The Asian continent being one of the strongest emission regions, CH_4 is exported to the North Pacific region more efficiently in July 2003. Depending on the location of measurement sites,

positive, neutral and negative CH_4 growth rate can be found in the North Pacific, most parts of Southern Hemisphere and the Asian continent, respectively.

The difference in integrated CH_4 MR for the whole troposphere is -1.03 ppb and 2.02 ppb for the month of July between 2004 and 2003, and in 2007 and 2006, respectively, even though change in emission used for ACTM simulation is not significant. We anticipate similar changes in methyl chloroform (MCF; CH_3CCl_3), due to atmospheric transport variabilities, that is used for deriving OH IAV (Rigby et al. 2008). An increase in MCF mixing ratio would result in decreased estimation of OH abundance, and thus a greater CH_4 emission. They derive an increase in CH_4 emission for 2003 for the interannually repeating OH case, but a weak sink is obtained for interannually varying OH case. By accounting for IAV in atmospheric transport alone one would derive a weak increase in CH_4 burden for July of 2003 relative to 2004 and that about the twice in July 2007 relative to 2006.

4. Conclusions and outlook

Simulations of CH_4 in atmosphere have been conducted using an AGCM-based chemistry transport model that incorporates simple loss mechanisms due to chemical reactions with OH and Cl radicals, and O^1D in the altitude range from the earth's surface to about 90 km. Based on these loss mechanisms and atmospheric burden of CH_4, the lifetime is estimated as 8.62 years, which compares well with the mean value of multiple state-of-the-arts CTMs. For generating short-term variations in PBL height region as well as the synoptic variations in model transport, the AGCM dynamics are nudged towards the NCEP AMIP II reanalysis winds and temperature at 6-hourly time intervals. The model results of atmospheric CH_4 simulations are compared with observations at more than 50 measurement sites on the earth's surface for validation of inter-hemispheric, latitudinal and longitudinal gradients. The comparison of gradients along both latitude and longitude allowed us to verify the overall validity of surface fluxes used in the control simulation, because the ACTM transport has been validated with respected to a non-reactive species (SF_6) in an earlier study (Patra et al. 2009). We found the country total emissions of 54, 54, 51, 47 and 41 Tg-CH_4 yr^{-1} (E2 scenario) from Brazil, USA, Russia, China and India, respectively, produced better model-observation agreements in comparison with that for E1 scenario.

The E2 emission scenario used in control run has been assessed further by comparing seasonal and synoptic variations at a set of three sites in the Indian subcontinent and Indian Ocean regions. Atmospheric CH_4 variability at hourly, synoptic, seasonal and interannual time scales have been derived from the digital filtered timeseries as observed and modeled at the surface sites depending on the measurement period and interval. Our results suggest that the growth rate IAVs are dominated by atmospheric transport in the tropics and forest fire emission in the high latitudes (sensitivity to other parameters were not conducted). The synoptic and diurnal variations are analyzed at 21 sites where continuous measurements are available. The highest correlation of the model-observation variabilities are found for the seasonal (at background sites) and diurnal (at continental sites mainly) cycles, followed by that for the synoptic and interannual variabilities. The good correlation of seasonal cycles at most sites confirms the validity of the combination of CH_4 surface flux distribution and chemical loss parameterization (by OH, O^1D and Cl) in ACTM. We have shown the importance of accurate CH_4 interhemispheric gradient (IHG) simulation for improved model-observation agreements in synoptic scale variations and seasonal cycles at tropical sites where IHG is the steepest.

Model-observation correlations (up to 0.7, i.e., capturing the variability of about 50%) are statistically significant and NSDs close to 1 at most sites (with 3 exceptions discussed in the text) for daily average CH_4 mixing ratios. Synoptic variations in CH_4 are modeled more realistically by ACTM compared to CO_2 at some sites, like MLO (Patra et al. 2008). Simulation of SF_6 synoptic variation at MLO also showed statistically significant correlation and NSD close to 1 (Patra et al. 2009), suggesting deficiencies in CO_2 fluxes rather than the model transport for poorer simulation of CO_2 synoptic variation by ACTM. The CH_4 diurnal amplitude simulated by ACTM also compares well at the land sites and shown to be caused entirely by diurnal variation in the PBL height, but the diurnal cycle at some coastal sites cannot be captured by ACTM simulation because of the coarse horizontal resolution.

We have tested the role of OH diurnal variations on CH_4 simulations that revealed the difference in CH_4 MRs corresponding to ACTM simulations

with or without OH is primarily arising from the temperature dependence of K_{OH} than the diurnal profile of OH. This and CH_4 chemical lifetime analysis imply that atmospheric transport plays the dominant role in controlling CH_4 variations at hourly, synoptic and monthly timescales. Our analysis of CH_4 budget suggests that total burden and loss in the whole troposphere did not vary significantly after the year 2000 at interannual timescales, while there were large positive/negative growth rate IAVs at regional scales near the earth's surface or at different layers of the atmosphere. This situation illustrates the role of dynamics-chemistry interaction for tropospheric CH_4 burden on annual basis. Because we have not considered IAV in CH_4 fluxes and OH abundance, a quantification of roles of different components (atmospheric dynamics, surface flux, chemical loss) in the CH_4 forward simulation cannot be made. Such an issue is probably better addressed in a multiple chemistry-transport modeling framework, where model transport vs. OH IAV sensitivity for CH_4 growth rate variability can be tested.

Acknowledgements

We thank Kazuyo Yamaji, Tazu Saeki and Sander Houweling for discussions on CH_4 emission and modeling frameworks, Kengo Sudo for allowing us to use the CHASER tropospheric chemistry model to prepare OH distributions, NIWA personnel for making their CH_4 measurements freely available, and Keith Lassey for informing about the interim calibration scale employed by NIWA. PKP acknowledges discussions with Mark Lawrence, Maarten Krol, Yugo Kanaya regarding the tropospheric OH distributions. We appreciate support of Hajime Akimoto for conducting this research at FRCGC. We thank two anonymous reviewers for their insightful comments and the editor for providing us with useful suggestions.

References

Aoki, S., T. Nakazawa, S. Murayama, and S. Kawaguchi, 1992, Measurements of atmospheric methane at the Japanese Antarctic Station, Syowa, *Tellus*, Ser. B, **44**, 273–281.

Arino, O., S. Plummer, and D. Defrenne, 2005, Fire disturbance: the ten years time series of the ATSR world fire atlas, Proceedings of the MERIS-AATSR workshop 2005, Frascati, Italy.

Bousquet, P., P. Ciais, J. B. Miller, E. J. Dlugokencky, D. A. Hauglustaine, C. Prigent, G. R. Van der Werf, P. Peylin, E. G. Brunke, C. Carouge, R. L. Langenfelds, J. Lathière, F. Papa, M. Ramonet, M. Schmidt, L. P. Steele, S. C. Tyler, and J. White, 2006, Contribution of anthropogenic and natural sources to atmospheric methane variability, *Nature*, **443**, 439–443, doi:10.1038/nature05132.

Chen, Y. -H., and R. G. Prinn, 2005, Atmospheric modeling of high- and low-frequency methane observations: Importance of interannually varying transport, *J. Geophys. Res.*, **110**, D10303, doi:10.1029/2004JD005542.

Chen, Y. -H., and R. G. Prinn, 2006, Estimation of atmospheric methane emissions between 1996 and 2001 using a three-dimensional global chemical transport model, *J. Geophys. Res.*, **111**, D10307, doi:10.1029/2005JD006058.

Cunnold, D. M., L. P. Steele, P. J. Fraser, P. G. Simmonds, R. G. Prinn, R. F. Weiss, L. W. Porter, S. O'Doherty, R. L. Langenfelds, P. B. Krummel, H. J. Wang, L. Emmons, X. X. Tie, and E. J. Dlugokencky, 2002, In situ measurements of atmospheric methane at GAGE/AGAGE sites during 1985–2000 and resulting source inferences, *J. Geophys. Res.*, **107**, doi:10.1029/2001JD001226.

Dentener, F., M. van Weele, M. Krol, S. Houweling, and P. van Velthoven, 2003, Trends and inter-annual variability of methane emissions derived from 1979–1993 global CTM simulations, *Atmos. Chem. Phys.*, **3**, 73–88.

Dentener, F., et al., 2006, The global atmospheric environment for the next generation, *Environ. Sci. Technol.*, **40**, 3586–3594.

Dlugokencky, E. J., K. A. Masarie, P. M. Lang, and P. P. Tans, 1998, Continuing decline in the growth rate of the atmospheric methane burden, *Nature*, **393**, 447–450.

Dlugokencky, E. J., S. Houweling, L. Bruhwiler, K. A. Masarie, P. M. Lang, J. B. Miller, and P. P. Tans, 2003, Atmospheric methane levels off: Temporary pause or a new steady-state?, *Geophys. Res. Lett.*, **30**, 1992, doi:10.1029/2003GL018126.

Dlugokencky, E. J., R. C. Myers, P. M. Lang, K. A. Masarie, A. M. Crotwell, K. W. Thoning, B. D. Hall, J. W. Elkins, and L. P. Steele, 2005, Conversion of NOAA atmospheric dry air CH_4 mole fractions to a gravimetrically prepared standard scale, *J. Geophys. Res.*, **110**, D18306, doi:10.1029/2005JD006035.

Etheridge, D., L. Steele, R. Francey, and R. Langenfelds, 1998, Atmospheric methane between 1000 A.D. and present: Evidence of anthropogenic emissions and climatic variability, *J. Geophys. Res.*, **103**, 15979–15993.

Ferretti, D. F., J. B. Miller, J. W. C. White, D. M. Etheridge, K. R. Lassey, D. C. Lowe, C. M. MacFarling Meure, M. F. Dreier, C. M. Trudinger, T. D. van Ommen, and R. L. Langenfelds, 2005, Unexpected

changes to the global methane budget over the past 2000 years, *Science*, **309**, 1714–1717, doi:10.1126/science.1115193.

Fiore, A. M., L. W. Horowitz, E. J. Dlugokencky, and J. J. West, 2006, Impact of meteorology and emissions on methane trends, 1990–2004, *Geophys. Res. Lett.*, **33**, L12809, doi:10.1029/2006GL026199.

Fung, I., J. John, J. Lerner, E. Matthews, M. Prather, L. P. Steele, and P. J. Fraser, 1991, Three-dimensional model synthesis of the global methane cycle, *J. Geophys. Res.*, **96**, 13,033–13,065.

Hein, R., P. J. Crutzen, and M. Heimann, 1997, An inverse modeling approach to investigate the global atmospheric methane cycle, Global Biogeochem. *Cycles*, **11**, 43–76.

Hansen, J., M. Sato, R. Ruedy, K. Lo, D. W. Lea, and M. Medina-Elizade, 2006, Global temperature change, *Proc. Natl. Acad. Sci.*, **103**, 14288–14293, doi:10.1073/pnas.0606291103.

Houghton, J. T., G. J. Jenkins, and J. J. Ephraums (eds.), 1990, Intergovernmental Panel on Climate Change (IPCC), *Scientific assessment of climate change—Report of working group I*, University Press, Cambridge, Great Britain.

Houweling, S., T. Kaminski, F. Dentener, J. Lelieveld, and M. Heimann, 1999, Inverse modeling of methane sources and sinks using the adjoint of a global transport model, *J. Geophys. Res.*, **104**, 26,137–26,160.

Houweling, S., F. Dentener, J. Lelieveld, B. Walter, and E. Dlugokencky, 2000, The modeling of tropospheric methane: How well can point measurements be reproduced by a global model?, *J. Geophys. Res.*, **105**, 8981–9002.

Houweling, S., T. Röckmann, I. Aben, F. Keppler, M. Krol, J. F. Meirink, E. J. Dlugokencky, and C. Frankenberg, 2006, Atmospheric constraints on global emissions of methane from plants, *Geophys. Res. Lett.*, **33**, L15821, doi:10.1029/2006GL026162.

Kanamitsu, et al., 2002, NCEP-DOE AMIP-II reanalysis (R-2), *Bull. Amer. Meteor. Soc.*, **83**, 1631–1643.

Kanaya, Y., R. Cao, H. Akimoto, M. Fukuda, Y. Komazaki, Y. Yokouchi, M. Koike, H. Tanimoto, N. Takegawa, and Y. Kondo, 2007, Urban photochemistry in central Tokyo: 1. Observed and modeled OH and HO 2 radical concentrations during the winter and summer of 2004, *J. Geophys. Res.*, **112**, D21312.

Krol, M., P. van Leeuwen, and J. Lelieveld, 1998, Global OH trend inferred from methyl chloroform measurements, *J. Geophys. Res.*, **103**, 10697–10711.

Langenfelds, R. L., R. J. Francey, B. C. Pak, L. P. Steele, J. Lloyd, C. M. Trudinger, and C. E. Allison, 2002, Interannual growth rate variations of atmospheric CO_2 and its $\delta^{13}C$, H_2, CH_4, and CO between 1992 and 1999 linked to biomass burning, *Global Biogeochem. Cycles*, **16**, 1048.

Law, R. M., W. Peters, C. Rödenbeck, et al., 2008, TransCom model simulations of hourly atmospheric CO_2: experimental overview and diurnal cycle results for 2002, Global Biogeochem. *Cycles*, **22**, GB3009.

Maksyutov, S., P. K. Patra, R. Onishi, T. Saeki, and T. Nakazawa, 2008, NIES/FRCGC Global Atmospheric Tracer Transport Model: Description, Validation, and Surface Sources and Sinks Inversion, *J. Earth Sim.*, **9**, 2–18.

Manning, M. R., D. C. Lowe, R. C. Moss, G. E. Bodeker, and W. Allan, 2005, Short-term variations in the oxidising power of the atmosphere, Nature, **436** (7053), 889–1064.

Matthews, E., and I. Fung, 1987, Methane emissions from natural wetlands: Global distribution, area, and ecology of sources, Global Biogeochem. *Cycles*, **1**, 61–86.

McCulloch, A., and P. M. Midgley, 2001, The history of methyl chloroform emissions: 1951–2000, *Atmos. Environ.*, **35**, 5311–5319.

Mikaloff-Fletcher, S. E., P. P. Tans, L. M. Bruhwiler, J. B. Miller, and M. Heimann, 2004, CH_4 sources estimated from atmospheric observations of CH_4 and its 13C/12C isotopic ratios: 2. Inverse modeling of CH_4 fluxes from geographical regions, Global Biogeochem. *Cycles*, **18**, GB4005, doi:10.1029/2004GB002224.

Morimoto, S., S. Aoki, T. Nakazawa, and T. Yamanouchi, 2006, Temporal variations of the carbon isotopic ratio of atmospheric methane observed at Ny Ålesund, Svalbard from 1996 to 2004, *Geophys. Res. Lett.*, **33**, L01807, doi:10.1029/2005GL024648.

Nakazawa, T., T. Machida, M. Tanaka, Y. Fujii, S. Aoki, and O. Watanabe, 1993, Differences of the Atmospheric CH_4 Concentration between the Arctic and Antarctic Regions in Pre-Industrial and Pre-Agricultural Era, *Geophys. Res. Lett.*, **20**, 943–946.

Nakazawa, T., M. Ishizawa, K. Higuchi, and N. B. A. Trivett, 1997, Two curve fitting methods applied to CO_2 flask data, *Environmetrics*, **8**, 197–218.

Olivier, J. G. J., and J. J. M. Berdowski, 2001, Global emissions sources and sinks, in *The Climate System*, edited by J. Berdowski, R. Guicherit, and B. J. Heij, A. A. Balkema Publishers/Swets & Zeitlinger Pub., Lisse, The Netherlands, ISBN 9058092550, pp. 33–78.

Patra, P. K., R. M. Law, W. Peters, C. Rödenbeck, M. Takigawa, et al., 2008, TransCom model simulations of hourly atmospheric CO_2: analysis of synoptic scale variations for the period 2002–2003, *Global Biogeochem. Cycles*, **22**, GB9013, doi:10.1029/2007GB003081.

Patra, P. K., M. Takigawa, G. S. Dutton, K. Uhse, K. Ishijima, B. R. Lintner, K. Miyazaki, and J. W. Elkins, 2009, Transport mechanisms for synoptic, seasonal and interannual SF_6 variations and "age" of air in the troposphere, *Atmos. Chem. Phys.*, **9**, 1209–1225.

Prinn, R. G., J. Huang, R. F. Weiss, D. M. Cunnold, P. J. Fraser, P. G. Simmonds, A. McCulloch, C. Harth, P. Salameh, S. O'Doherty, R. H. J. Wang, L. Porter, and B. R. Miller, 2001, Evidence for substantial variations of atmospheric hydroxyl radicals in the past two decades, *Science*, **292**, 1882–1888.

Rasmussen, R. A., and M. A. K. Khalil, 1984, Atmospheric methane in recent and ancient atmospheres: concentrations, trends, and interhemispheric gradient, *J. Geophys. Res.*, **89**, 599–605.

Rigby, M., et al., 2008, Renewed growth of atmospheric methane, *Geophys. Res. Lett.*, **35**, L22805, doi:10.1029/2008GL036037.

Saeki, T., T. Nakazawa, M. Tanaka, and K. Higuchi, 1998, Methane Emissions Deduced from a Two-Dimensional Atmospheric Transport Model and Surface Measurements, *J. Meteorol. Soc. Japan*, **76**, 307–324.

Sander, S. P., R. R. Friedl, D. M. Golden, M. J. Kurylo, G. K. Moortgat, P. H. Wine, A. R. Ravishankara, C. E. Kolb, M. J. Molina, B. J. Finlayson-Pitts, R. E. Huie, and V. L. Orkin, 2006, Chemical Kinetics and Photochemical Data for Use in Atmospheric Studies, Evaluation Number 15, JPL Publication 06-2, Jet Propulsion Laboratory, California Institute of Technology, Pasadena, CA.

Simpson, I. J., F. S. Rowland, S. Meinardi, and D. R. Blake, 2006, Influence of biomass burning during recent fluctuations in the slow growth of global tropospheric methane, *Geophys. Res. Lett.*, **33**, L22808, doi:10.1029/2006GL027330.

Steele, L. P., E. J. Dlugokencky, P. M. Lang, P. P. Tans, R. C. Martin, and K. A. Masarie, 1992, Slowing down of the global accumulation of atmospheric methane during the 1980s, *Nature*, **358**, 313–316.

Stevenson, D. S., et al., 2006, Multimodel ensemble simulations of present-day and near-future tropospheric ozone, *J. Geophys. Res.*, **111**, D08301, doi:10.1029/2005JD006338.

Sudo, K., M. Takahashi, J. Kurokawa, and H. Akimoto, 2002, CHASER: A global chemical model of the troposphere 1. Model description, *J. Geophys. Res.*, **107**, 4339, doi:10.1029/2001JD001113.

Takigawa, M., M. Takahashi, and H. Akiyoshi, 1999, Simulation of ozone and other chemical species using a Center for Climate System Research/National Institute for Environmental Studies atmospheric GCM with coupled stratospheric chemistry, *J. Geophys. Res.*, **104**, 003–018.

Tohjima, Y., T. Machida, M. Utiyama, M. Katsumoto, Y. Fujinuma, and S. Maksyutov, 2002, Analysis and presentation of in situ atmospheric methane measurements from Cape Ochi-ishi and Hateruma Island, *J. Geophys. Res.*, **107**, 4148, doi:10.1029/2001JD001003.

van der Werf, G. R., J. T. Randerson, L. Giglio, G. J. Collatz, P. S. Kasibhatla, and A. F. Arellano Jr, 2006, Interannual variability in global biomass burning emissions from 1997 to 2004, *Atmos. Chem. Phys.*, **6**, 3423–3441.

Walter, B. P., M. Heimann, and E. Matthews, 2001, Modeling modern methane emissions from natural wetlands 2. Interannual variations 1982–1993, *J. Geophys. Res.*, **106**, 207–219.

Wang, J. S., J. A. Logan, M. B. McElroy, B. N. Duncan, I. A. Megretskaia, and R. M. Yantosca, 2004, A 3-D model analysis of the slowdown and interannual variability in the methane growth rate from 1988 to 1997, Global Biogeochem. *Cycles*, **18**, GB3011, doi:10.1029/2003GB002180.

Warwick, N. J., S. Bekki, K. S. Law, E. G. Nisbet, and J. A. Pyle, 2002, The impact of meteorology on the international growth rate by atmospheric methane, *Geophys. Res. Lett.*, **29**, 1947, doi:10.1029/2002GL015282.

WDCGG (2007), WMO World Data Centre for Greenhouse Gases, Japan Meteorological Agency, Tokyo (data available at http://gaw.kishou.go.jp/wdcgg.html).

Worthy, D. E. J., I. Levin, N. B. A. Trivett, A. J. Kuhlmann, J. F. Hopper, and M. K. Ernst, 1998, Seven years of continuous methane observations at a remote boreal site in Ontario, Canada, *J. Geophys. Res.*, **103**, 15,995–16,007.

Yamaji, K., T. Ohara, and H. Akimoto, 2003, A country-specific, high-resolution emission inventory for methane from livestock in Asia in 2000, *Atmos. Environ.*, **37**, 4393–4406.

Yan, X., H. Akiyama, K. Yagi, and H. Akimoto, 2008, Global estimations of an inventory and mitigation potentials of methane emissions from rice cultivation by using methodology of the 2006 IPCC Guidelines, Global Biogeochem. *Cycles*, submitted.